JCI The Journal of Clinical Investigation

Sensory nerves regulate mesenchymal stromal cell lineage commitment by tuning sympathetic tones

Bo Hu, … , Wen Yuan, Xu Cao

J Clin Invest. 2020. https://doi.org/10.1172/JCI131554.

Research In-Press Preview **Bone biology** **Stem cells**

Graphical abstract

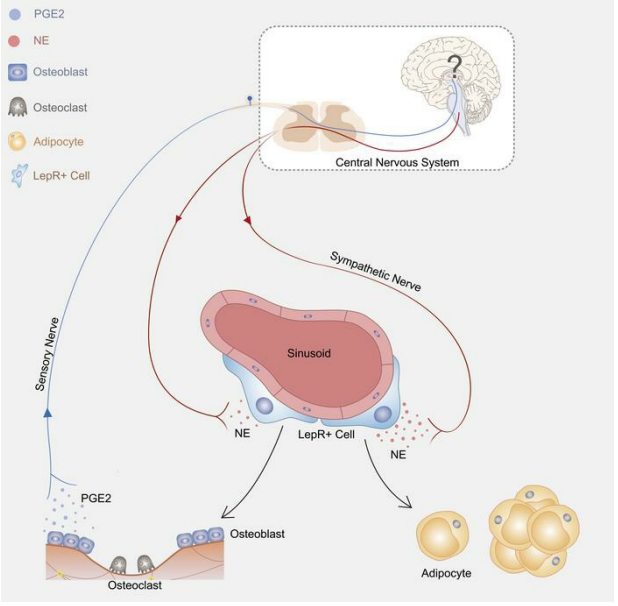

Sensory Nerves Regulate Mesenchymal Stromal Cell Lineage Commitment by Tuning Sympathetic Tones

Bo Hu[1,2,†], Xiao Lv[1,3,†], Hao Chen[1], Peng Xue[1], Bo Gao[1], Xiao Wang[1], Gehua Zhen[1], Janet L. Crane[1], Dayu Pan[1], Shen Liu[1], Shuangfei Ni[1], Panfeng Wu[1], Weiping Su[1], Xiaonan Liu[1], Zemin Ling[1], Mi Yang[1], Ruoxian Deng[1], Yusheng Li[1], Lei Wang[1], Ying Zhang[2], Mei Wan[1], Zengwu Shao[3], Huajiang Chen[2], Wen Yuan[2*] and Xu Cao[1*]

[1]Department of Orthopaedic Surgery, The Johns Hopkins University, Baltimore, MD 21205, USA.

[2]Section of Spine Surgery, Department of Orthopaedics, Changzheng Hospital, Second Military Medical University, Shanghai, P. R. China.

[3]Department of Orthopaedics, Union Hospital, Tongji Medical College, Huazhong University of Science and Technology, Wuhan, P. R. China

Conflict of Interests statement

The authors have declared that no conflict of interest exists.

[†] These authors contributed equally to this article.

[*] Correspondence should be addressed to Xu Cao, Department of Orthopaedic Surgery, The Johns Hopkins University, 720 Rutland Avenue, Baltimore, MD 21205 (Tel: 205 643 4333, email: xcao11@jhmi.edu). Or to Wen Yuan, Section of Spine Surgery, Department of Orthopaedics,

Changzheng Hospital, Second Military Medical University, 415 Fengyang Rd, Huangpu District, Shanghai, P. R. China. (Tel: 86 21 81885630, email: yuanwenspine@126.com)

Abstract

Sensory nerve was recently identified as being involved in regulation of bone mass accrual. We previously discovered that PGE2 secreted by osteoblastic cells could activate sensory nerve EP4 receptor to promote bone formation by inhibiting sympathetic activity. However, the fundamental units of bone formation are active osteoblasts, which originate from mesenchymal stromal/stem cells (MSCs). Here, we found that after sensory denervation, knockout of the EP4 receptor in sensory nerves, or knockout of cyclooxygenase-2 (COX2) in osteoblasts could significantly promote adipogenesis and inhibit osteogenesis in adult mice. Furthermore, injection of SW033291 (a small molecule that locally increases PGE2 level) or propranolol (a beta-blocker) significantly promoted osteogenesis and inhibited adipogenesis. This effect of SW033291, but not propranolol, was abolished in conditional EP4 knockout mice under normal conditions or in the bone repair process. We conclude that the PGE2-EP4 sensory nerve axis could regulate MSCs differentiation in bone marrow of adult mice.

Key words: EP4 receptor, prostaglandin E2, sensory nerve, mesenchymal stromal/stem cells, sympathetic nerve

Introduction

Sensory nerves are innervated in various organs and tissues, such as skin, lung, kidney, liver, and bone. These nerves sense stimuli, such as pain, itch, temperature, taste, and odor (1,2). The function of sensory nerves is essential for collecting information from both internal and external environments, thus helping individuals adapt to their surroundings and protect themselves from threats (3). Recent evidence has shown that sensory nerves also participate in inflammation, immunity, hematopoiesis, and bone metabolism (4,5). Fukuda et al. first reported that loss of sensory nerves could impair bone mass accrual (5). Conversely, Takeda et al. found that bone metabolism was regulated by the sympathetic nerve system (6). Our previous report showed that sensory nerve could detect the bone-forming "signal" from osteoblastic cells and further tune down sympathetic activity via the central nervous system, thus control bone homeostasis (7).

The bone-forming "signal" mentioned above is prostaglandin E2 (PGE2). We find that PGE2 activates the EP4 receptor in sensory nerves to promote bone formation via the central nervous system (7). PGE2 is synthesized by the enzyme cyclooxygenase (COX), is degraded by the enzyme 15-hydroxyprostaglandin dehydrogenase (15-PGDH) (8,9), and is well known for its roles in inflammation and pain induction (8,10,11). PGE2 also could potent induce bone formation, promote tissue regeneration, and facilitate bone repair (12,13). Direct injection of PGE2 failed as a treatment for osteoporosis and did not increase bone mass in mice (14). These outcomes might be caused by its broad targets, which cause adverse effects. However, a new small molecule, SW033291, was developed by Zhang et al. and may inhibit 15-PGDH activity, thus indirectly increasing PGE2 accumulation in certain microenvironments (12). Their group also showed that

SW033291 possessed tissue regeneration–boosting ability, which markedly promoted liver, intestine, and hematopoiesis regeneration after injury (12). Our group also showed that SW033291 injection could directly increase bone mass and promote bone regeneration via the EP4-sensory nerve axis in mice (7). However, we identified the upstream "regulator," but not the downstream "effector" of this axis.

The adult skeleton is continuously being formed and resorbed, starting in utero and continuing throughout adulthood (15). This skeletal remodeling is accomplished by precise coordination between resorptive osteoclasts and bone-forming osteoblasts (16,17). The sequence in bone remodeling cycles starts with osteoclastic bone resorption, followed by osteoblastic bone formation (18), which relies on constant supplies of osteoblast differentiation ascended from bone marrow mesenchymal stromal/stem cells (MSCs) (19,20). Bone marrow MSCs, a subset of mesenchymal cells, possess self-renewal and multiple-lineage differentiation capability to produce adipocyte, osteoblast, and chondrocyte in bone tissue (21-24). MSCs reside primarily in their bone marrow niche in a quiescent stage and become active when the niche is stimulated by factors such as injury, inflammation, or medicine intake (25-27). The MSCs niche and microenvironment determine the cells' commitment and self-renewal for bone homeostasis. An impaired niche or microenvironment alters MSCs commitment, which has been reported in human diseases such as tissue fibrosis, malignant hematopoiesis, and osteoporosis (28-30). Recent studies found that sympathetic nerves could serve as an MSC niche component in bone marrow and regulate interactions between MSCs and hematopoietic stem cells, thus maintaining normal hemopoiesis (31,32).

In our study, we investigated whether EP4-PGE2 in sensory nerves regulate bone mass accrual through direct control of commitment of MSCs by tuning down sympathetic nerve activity. We show that adipogenesis is significantly increased, whereas osteogenesis is markedly decreased in sensory denervation mice, sensory nerve EP4 knockout mice, and osteoblast COX2 knockout mice. Elevation of PGE2 by SW033291 inhibits adipogenesis and promotes osteogenesis, bone regeneration, and bone fracture healing in wild type (WT) mice, but not in the knockout mice models. We conclude that MSCs differentiation is regulated by the PGE2-EP4 sensory nerve axis in adult mice.

Results

Sensory nerve denervation induces adipogenesis at expenses of osteogenesis in adult mice.

To create a sensory nerve denervation model, we crossed *Advilin-Cre* mice with nerve growth factor receptor *TrkA* floxed ($TrkA^{wt}$) mice to generate $TrkA_{Avil}^{-/-}$ mice according to our previous work (7). Bone volume fraction (BV/TV) and trabecular thickness (Tb.Th) significantly decreased in 3-month-old $TrkA_{Avil}^{-/-}$ mice relative to their WT littermates, whereas no significant changes in these bone parameters were observed in 1-month-old $TrkA_{Avil}^{-/-}$ mice (Figure 1A-C, Supplemental Figure 1A-C), suggesting sensory nerve regulation of bone homeostasis, primarily in adult mice. Fat was significantly increased in the bone marrow of 3-month-old $TrkA_{Avil}^{-/-}$ mice compared with the WT controls, as evidenced by a markedly higher number of adipocytes and fat droplets in decalcified femurs stained with osmium tetroxide (OsO_4) (Figure 1D-F). Immunostaining of osteocalcin (OCN) for osteogenesis with perilipin for adipogenesis showed a significant increase

in the number of adipocytes and decrease in the number of osteoblasts in 3-month-old $TrkA_{Avil}^{-/-}$ mice relative to their WT littermates (Figure 1G-I). Colony-forming-unit fibroblast (CFU-F), adipocyte (CFU-AD), and osteoblast (CFU-OB) assays with bone marrow cells showed a significant increase in adipogenesis and decreases in osteogenesis and CFU-Fs (Figure 2A-D) in $TrkA_{Avil}^{-/-}$ mice relative to WT littermates. Consistently, bone marrow cell expression of adipogenic marker peroxisome proliferator-activated receptor γ (Pparg), CCAAT/enhancer-binding protein α (Cebpa), and fatty acid–binding protein 4 (Fabp4) increased significantly, whereas the osteogenic marker alkaline phosphatase (Alp), Collagen type Ia (Col1a1), and Runt-related transcription factor 2 (Runx2) expression decreased (Supplemental Figure 1D and E).

These results prompted us to test whether this alteration is caused by sensory nerve regulation of MSCs. Flow cytometry analysis showed that $CD45^{-}CD31^{-}Sca1^{+}CD24^{-}$ adipogenic progenitor cells (APCs) significantly increased, and $CD45^{-}CD31^{-}Sca1^{-}PDGFR\alpha^{+}$ ($P\alpha^{+}$) osteogenic progenitor cells (OPCs) decreased (Figure 2E, F and H). Importantly, the population of $CD45^{-}CD31^{-}Sca1^{+}CD24^{+}$ MSCs also decreased (Figure 2E and G), consistent with the CFU-F results (Figure 2A). Moreover, $BrdU^{+}$ OPCs and $BrdU^{+}$ MSCs decreased significantly in 3-month-old $TrkA_{Avil}^{-/-}$ mice relative to their WT littermates, whereas $BrdU^{+}$ APCs remained unchanged (Supplemental Figure 2A-D), consistent with the CFU-F result of relative sorted cell population (Supplemental Figure 3A-C). Also, sorted MSCs showed increased adipogenic potential and decreased osteogenic capability in $TrkA_{Avil}^{-/-}$ mice relative to controls (Supplemental Figure 3D-M). These data together suggest that sensory denervation lead to increase of bone marrow adipogenesis activity in adult mice. Similar results were obtained in an inducible sensory

denervation model in $iDTR_{Avil}^{fl/-}$ mice by crossing *Advillin-Cre* mice with $iDTR^{wt}$ mice according to the methods used in our previous study (7). The results showed that marrow fat was significantly increased in the bone marrow of $iDTR_{Avil}^{fl/-}$ mice 4 weeks after injection of diphtheria toxin (DTX) relative to vehicle-treated mice, as evidenced by markedly more adipocytes and fat droplets in decalcified femurs stained with OsO_4 (Figure 3A-C). The frequency of MSCs and OPCs decreased, whereas the frequency of APCs increased after DTX treatment relative to vehicle treatment in flow cytometry analysis (Figure 3D-G). Immunostaining of OCN with perilipin also showed a significant increase in adipocytes and decrease in osteoblasts after DTX treatment (Figure 3H-J). Taken together, these data demonstrate that sensory nerve is essential to maintain MSCs and balance their commitment between osteoblast and adipocytes.

Deletion of the EP4 Receptor in Sensory Nerve Promotes Adipogenesis and Inhibits Osteogenesis in Adult Mice

We have shown that the EP4 receptor in sensory nerve is essential for maintaining normal bone mass in adult mice (7). EP4 knockout ($EP4_{Avil}^{-/-}$) mice showed significant decreases in BV and Tb.Th relative to their WT littermates (Figure 4A-C, Supplemental Figure 4A-C). Marrow fat was significantly increased in the bone marrow of $EP4_{Avil}^{-/-}$ mice relative to WT controls, as evidenced by markedly more adipocytes and fat droplets in decalcified femurs stained with OsO_4 (Figure 4D-F). To test whether differentiation of MSCs could also be regulated by the EP4 receptor in sensory nerve, we injected PGE2 degradation enzyme (15-PGDH) inhibitor SW033921 into $EP4_{Avil}^{-/-}$ mice and their WT littermates. Injection of SW033291 significantly increased the number of osteoblasts

and decreased the number of adipocytes in WT mice, and these effects were absent in $EP4_{Avil}^{-/-}$ mice (Figure 4G-I), indicating that PGE2-EP4 sensory nerve axis regulates MSCs differentiation. Moreover, MSCs isolated from $EP4_{Avil}^{-/-}$ mice showed an increase of CFU-AD, and a decrease in CFU-OB and CFU-F capability compared with MSCs from their WT littermates (Figure 4J-M, Supplemental Figure 3). The expression of adipogenic markers Pparg, Cebpa, and Fabp4 significantly increased, whereas the expression of osteogenic markers Alp, Col1a1, and Runx2 significantly decreased in MSCs isolated from $EP4_{Avil}^{-/-}$ mice relative to their WT mice in quantitative real-time polymerase reaction chain (qPCR) analysis (Supplemental Figure 4D and E). The frequency of APCs ($CD45^{-}CD31^{-}Sca1^{+}CD24^{-}$) increased, whereas the frequencies of OPCs ($CD45^{-}CD31^{-}Sca1^{-}Pa^{+}$) and MSCs ($CD45^{-}CD31^{-}Sca1^{+}CD24^{+}$) decreased (Figure 4N-Q) in $EP4_{Avil}^{-/-}$ mice relative to WT littermates. The $BrdU^{+}$ OPCs and $BrdU^{+}$ MSCs decreased in $EP4_{Avil}^{-/-}$ mice compared with control mice, whereas the $BrdU^{+}$ APCs showed no significant change in $EP4_{Avil}^{-/-}$ mice relative to WT littermates (Supplemental Figure 2E-H). These results indicate that the EP4 receptor in sensory nerve is essential for sensory nerve regulation of MSCs differentiation.

PGE2 Derived from Osteoblasts Regulates the Differentiation of MSCs through Sensory Nerve EP4 by Regulating Sympathetic Tone

We have shown that PGE2 derived from osteoblasts is primarily involved in sensory nerve regulation of bone formation (7). $COX2_{osteocalcin\ (OCN)}^{-/-}$ mice showed significant decreases in BV and Tb.Th relative to their WT littermates (Figure 5A-C, Supplemental Figure 5A-C). Marrow fat

was significantly increased in the bone marrow of $COX2_{OCN}^{-/-}$ mice relative to WT controls, as evidenced by markedly more adipocytes and fat droplets in decalcified femurs stained with OsO_4 (Figure 5D-F). To examine whether PGE2 secreted from osteoblasts also regulates the differentiation of MSCs, we injected SW033291 into $COX2_{OCN}^{-/-}$ mice and their WT littermates. We found that the effects of SW033291 on osteogenesis induction and adipogenesis inhibition were reduced in $COX2_{OCN}^{-/-}$ mice (Figure 5G-I), indicating that the PGE2 derived from osteoblasts in the bone remodeling microenvironment is essential in the regulation of MSCs differentiation. These results were confirmed in CFU-F, CFU-OB, and CFU-AD assays (Figure 5J-M, Supplemental Figure 3) and qPCR analysis of osteogenic and adipogenic markers (Supplemental Figure 5D and E). Moreover, flow cytometry analysis also demonstrated decreased frequency of OPCs and MSCs and increased frequency of APCs in $COX2_{OCN}^{-/-}$ mice (Figure 5N-Q). BrdU-incorporated OPCs and MSCs were decreased, whereas BrdU-incorporated APCs were not affected (Supplemental Figure 2I-L). These results indicate that PGE2-derived from osteoblasts in the bone remodeling microenvironment act on sensory nerve for differentiation of MSCs.

We have shown that PGE2 activation of sensory nerve regulates bone formation by tuning down sympathetic tone (7). And we also found that obstruction of PGE2-EP4-sensory nerve axis could induce increased sympathetic activity (Supplemental Figure 6), in this case, to further test whether sympathetic nerve also regulates MSCs differentiation, we injected propranolol into $EP4_{Avil}^{-/-}$ mice and their WT littermates. Propranolol rescued the bone loss in $EP4_{Avil}^{-/-}$ mice (Supplemental Figure 7A-C). Importantly, propranolol promoted osteogenesis and inhibited adipogenesis in $EP4_{Avil}^{-/-}$ mice (Supplemental Figure 7D-F). To further demonstrate the effect of

specified sympathetic adrenoceptors in sensory nerve regulated MSCs differentiation, we injected selective β1 adrenoceptor antagonist (Atenolol), β2 adrenoceptor antagonist (ICI118551) and β3 adrenoceptor antagonist (SR59230A) into $EP4_{Avil}^{-/-}$ mice and their WT littermates, respectively, the results showed that only β2 adrenoceptor antagonist injection showed similar effect comparable to propranolol injection, which it rescued the bone loss and enhanced adipogenesis phenotype of $EP4_{Avil}^{-/-}$ mice (Supplemental Figure 8). Sympathetic β2 adrenoceptor antagonist's attenuation of sensory nerve regulation of bone formation suggests sympathetic tone regulation on MSCs.

LepR$^+$ MSCs are the Major Source of Increased Adipocytes, which are Regulated by the PGE2-EP4 Sensory Nerve Axis

Previous results showed that the frequencies of MSCs and OPCs decreased, whereas the frequency of APCs increased. However, the specific in vivo population of MSCs that responds to sensory nerve regulation and the origin of these increased adipocytes in sensory nerve denervated mice were still elusive. To address this question, we used Leptin Receptor (LepR)-cre mouse line to fate mapping MSCs in vivo according to previous reports (33), we crossed LepR-cre with Rosa26-YFP mice to generate *LepR-cre;YFP* mice for in vivo MSCs fate mapping assay. Capsaicin or vehicle was injected into 3-month-old *LepR-cre;YFP* mice for 1 week to generate the induced sensory denervation model, and mice were euthanized after another 2 weeks. The sensory denervation efficacy of capsaicin injection was comparable to $TrkA_{Avil}^{-/-}$ mice, as verified by von frey and hot plate test (Supplemental Figure 9A-C). Micro–computed tomography (μCT) analysis showed that

BV/TV and Tb.Th were significantly reduced in the capsaicin-injection group compared with vehicle group (Figure 6A-C). The marrow fat was significantly increased in the bone marrow of capsaicin-injected mice relative to vehicle controls as evidenced by markedly more adipocytes and fat droplets in decalcified femurs stained with OsO_4 (Figure 6D-F). Adipogenesis was increased and osteogenesis was decreased after capsaicin injection relative to the control group (Figure 6G-I). Sensory nerve marker calcitonin gene-related peptide (CGRP) immunostaining showed a significant decrease in $CGRP^+$ sensory nerves in bone marrow, which validated the sensory denervation efficacy of capsaicin injection (Figure 7A and B). In vivo fate mapping assay showed that YFP^+ adipocytes were significantly increased after sensory denervation. Propranolol, not SW033291, could lower the number of YFP^+ adipocytes, which were induced by sensory denervation (Figure 7C and D). These data together indicate that $LepR^+$ MSCs respond to sensory nerve denervation and commit to adipogenic differentiation, while yielding osteogenesis of MSCs.

Impairment of EP4 in Sensory Nerve Promotes Adipogenesis and Attenuates Bone Regeneration

To examine whether sensory nerve also regulates bone regeneration, we created a bone marrow ablation bone regeneration model in *LepR-cre;YFP* mice with impairment of sensory nerve by injection with capsaicin or vehicle. Bone regeneration was significantly reduced with sensory denervation by injection of capsaicin in μCT analysis, safranin-O/fast green (SO/FG) staining (red, cartilage; green, bone), Masson staining (red, muscle and cytoplasm; blue, bone) and Movat pentachrome staining (yellow, bone; green, cartilage/endochondral ossification; red, bone marrow)

(Figure 8A-C and Supplemental Figure 10A). Co-staining of perilipin with OCN showed active osteoblast differentiation with few perilipin$^+$ adipocytes during bone regeneration in the vehicle group. In contrast, while OCN$^+$ osteoblasts were less detectable, adipocytes increased significantly with injection of capsaicin (Figure 8D-F). Again, fate mapping assay showed that increased adipocytes were largely YFP$^+$ (Figure 8G and H). We further tested whether EP4 in the sensory nerve mediates bone regeneration by deleting EP4 in the sensory nerve of $EP4_{Avil}^{-/-}$ mice. Bone regeneration decreased significantly in $EP4_{Avil}^{-/-}$ mice relative their WT littermates (Figure 8I and J). SW033291 stimulated bone regeneration, and this effect was attenuated in $EP4_{Avil}^{-/-}$ mice (Figure 8I and J). Moreover, the number of osteoblasts increased and the number of adipocytes decreased in the bone regenerative region of WT mice treated with SW033291. In contrast, the number of adipocytes increased and the number of osteoblasts decreased in the bone regenerative region of $EP4_{Avil}^{-/-}$ mice relative to their WT littermates (Figure 8K-M). We also tested whether the EP4 receptor in LepR$^+$ MSCs is involved in sensory nerve regulation of bone formation. We crossed *LepR-cre* mice with $EP4^{wt}$ mice to generate $EP4_{LepR}^{-/-}$ descendants. We observed no significant changes in bone parameters in either 1-month-old or 3-month-old $EP4_{LepR}^{-/-}$ mice relative to their WT littermates (Supplemental Figure 11A-C). There were no significant differences in marrow fat, adipogenesis, or osteogenesis between $EP4_{LepR}^{-/-}$ mice and their WT littermates, as shown by μCT analysis of decalcified femurs stained with OsO_4 (Supplemental Figure 11D-F). Both $EP4_{LepR}^{-/-}$ mice and their WT littermates showed decreased adipogenesis and increased osteogenesis with injection of SW033291 (Supplemental Figure 11G-I). In addition, we also eliminated EP4 expression in osteoblasts by crossing OCN-cre mice with $EP4^{wt}$ mice to

generate $EP4_{Ocn}^{-/-}$ descendants, however, consistent with $EP4_{LepR}^{-/-}$ mice, $EP4_{Ocn}^{-/-}$ mice showed no bone or MSCs alteration relative to their WT littermates (Supplemental Figure 12A-E). These results indicate that EP4 in sensory nerves, not in MSCs or osteoblasts, regulates differentiation of MSCs during bone regeneration.

Impairment of EP4 in Sensory Nerve Interrupts Bone Fracture Healing

To examine whether EP4 in sensory nerve regulates bone fracture healing, we created a bone fracture model in *LepR-cre;YFP* mice with sensory nerve denervation by injecting capsaicin or vehicle. Injection of capsaicin reduced BV relative to the vehicle group in μCT analysis (Figure 9A-C), and bone formation was significantly lower in the capsaicin group, as shown by SO/FG staining (red, cartilage; green, bone) (Figure 9D). Masson staining (red, muscle and cytoplasm; blue, bone) and Movat pentachrome staining (yellow, bone; green, cartilage/endochondral ossification; red, bone marrow) showed that bone callus volume was also significantly decreased with injection of capsaicin (Figure 9D and Supplemental Figure 10B). As expected, co-staining of perilipin with OCN showed that OCN^+ osteoblasts were less detectable, whereas adipocytes increased significantly with injection of capsaicin (Figure 9E-G). Importantly, the increased adipocytes were primarily YFP^+, indicating they were descendants of $LepR^+$ cells (Figure 9H-I). We then performed bone fracture surgery in $EP4_{Avil}^{-/-}$ mice and their WT littermates to examine whether EP4 signaling mediates sensory nerve regulation. BV and formation were significantly reduced in the bone healing region of $EP4_{Avil}^{-/-}$ mice relative to their WT littermates (Figure 7J-N). Injection of SW033291 stimulated bone formation in the bone healing region of WT mice, but

such effects were absent in $EP4_{Avil}^{-/-}$ mice (Figure 10A-E). Moreover, SW033291 increased bone callus formation in WT mice was absent in $EP4_{Avil}^{-/-}$ mice, as shown by SO/FG, Masson staining and Movat pentachrome staining (Figure 10F and Supplemental Figure 10C). To determine whether sensory nerve stimulated the healing of bone fracture by regulation of MSCs differentiation, we co-immunostained sections of the fracture region with perilipin and OCN. The number of adipocytes increased significantly in $EP4_{Avil}^{-/-}$ mice relative to their WT littermates, with or without injection of SW033291, whereas SW033291 significantly increased the number of OCN^+ osteoblasts in the bone healing region of WT mice, but such effects were absent in $EP4_{Avil}^{-/-}$ mice (Figure 10G-I). Taken together, these results indicate that sensory nerve regulates osteoblast differentiation of MSCs for bone fracture healing through PGE2/EP4 signaling.

Discussion

Bone marrow MSCs differentiate into osteoblasts, adipocytes, and chondrocytes to maintain bone integrity (22-24). The maintenance of MSCs and its potential commitment to different cell lineages is essential to bone homeostasis (15,21,34). Notably, recent studies also characterized that skeletogenic cells which could differentiate to downstream progenitors of bone, cartilage and stromal tissue as skeletal stem cells (35-40). The MSCs committed as progenitors, including OPCs and APCs, could further differentiate into mature osteoblasts and adipocytes (33,41). Plentiful markers have been developed to mark the MSCs or their descendants for accurate analysis (42-46). A previous study showed that $CD45^-CD31^-Sca1^+CD24^+$ MSCs occupied more than 90% of the colonies formed with a tri-lineage differentiation capability assay (33). In the

present study, we used $CD45^{-}CD31^{-}Sca1^{+}CD24^{+}$ to mark MSCs, $CD45^{-}CD31^{-}Sca1^{+}CD24^{-}$ to mark APCs, and $CD45^{-}CD31^{-}Sca1^{-}PDGFR\alpha^{+}(P\alpha^{+})$ to mark OPCs. We found that sensory nerve regulates the fate of MSCs by tuning sympathetic nerve tones by binding the bone-forming signal PGE2 to the EP4 receptor, providing the first direct evidence of sensory nerve as a niche of mammalian stem cells.

The frequency and CFU-F ability of MSCs were impaired in sensory denervation mice, which increased their potential for adipogenesis and decreased osteogenesis. We have reported that sensory nerve could detect bone density by a local "sensor," PGE2, released by osteoblastic cells, sensing internal organ signals for bone homeostasis (7). Moreover, the abundance of MSCs significantly decreased in sensory denervation mice, suggesting that sensory nerve function as niche in maintenance of MSCs. We have shown that sensory nerve transmits bone-forming signals by tuning down the sympathetic nerve tone for osteoblasts bone formation (7). In addition, we also eliminated the possibility that osteocytic PGE2 might also involve in sensory nerve regulation on MSCs (Supplemental Figure 12G-L). Sympathetic tone is fulfilled by releasing norepinephrine and epinephrine, and an increase in epinephrine level could cause decreased bone formation (47,48). Epinephrine has been shown to strongly induce stem cells adipogenic commitment (49). Therefore, sensory nerve serves as a niche for MSCs, likely through control of epinephrine release of sympathetic tone. However, other sensory nerve secretory factors may also be involved in the maintenance of MSCs. Sensory nerve could also secrete neuropeptides, such as substance P, vasoactive intestinal peptide (50), and CGRP, which has been shown to promote osteoblast activity (51).

316 Deletion of the EP4 receptor in sensory nerve produced similar effects on bone formation
317 and MSCs as seen in sensory denervation mice. EP4 belongs to the PGE2 receptor family, which
318 consists of 4 receptors: EP1–EP4 (52). All 4 EPs have been globally knocked out, but only EP4
319 knockout mice have bone phenotype, providing evidence of a pivotal role of EP4 in PGE2-induced
320 bone formation (53). PGE2 has been shown to promote osteoblast differentiation and has even
321 been used as an anabolic bone formation drug in a clinic trial. Deletion of EP4 receptor in
322 osteoblast lineage cells did not show significant bone phenotype (54). Knockout of EP4 in sensory
323 nerve increased adipogenesis and decreased osteogenesis and the CFU-F ability of MSCs.
324 Discovery of the role of EP4 in sensory nerve regulation of MSCs' differentiation indicates a
325 possible mechanism for PGE2-induced bone formation. Moreover, mice with conditional knockout
326 of EP4 in $LepR^{+}$ lineage cells had no bone phenotype and still positively responded to SW033921
327 treatment, which it could potent stimulate bone formation (Supplemental Figure 13). Thus, PGE2
328 stimulates bone formation by activation of EP4 in sensory nerve regulation of MSCs. Concerning
329 whether this regulatory axis also functioning in other bones or metabolic systems, we did not find
330 any effect of PGE2-EP4-sensory nerve axis in mandible metabolism (Supplemental Figure 13),
331 this might due to the different MSCs population are responsible for bone metabolism in different
332 bones (7,33,55). Interestingly, we found that $EP4_{Avil}^{-/-}$ mice possessed significant higher body fat
333 mass compared with their wild type littermates (Supplemental Figure 14), this evidence indicates
334 that PGE2-EP4-sensory nerve signaling indeed have a potential impact on body fat and metabolic
335 systems, and this underlying mechanism will be our next research target.
336 $CD45^{-}CD31^{-}Sca1^{+}CD24^{+}$ MSCs were used in our flow cytometry analysis (33). LepR has

been reported to mark MSCs in adult mouse bone marrow, and LepRcre is effective for in vivo fate mapping of MSCs (42,43). Nearly 13% of $LepR^+$ stromal cells are $Sca1^+$, and all $Sca1^+$ stromal cells are $LepR^+$ (42), which indicates that $LepR^+$ MSCs contain all $CD45^-CD31^-Sca1^+CD24^+$ MSCs. Furthermore, $LepR^+$ stromal cells mark nearly 90% of bone marrow adipocytes in adult mice (42). Most recently, Baryawno et al. performed single cell sequencing to build bone marrow cellular atlas of taxonomy and showed that $LepR^+$ stromal cells formed a major cluster with ability to partition into osteolineage and adipolineage cells (56). Therefore, LepRcre could effectively trace cells in both osteoblast and adipocyte lineages in fate mapping in a similar population of $CD45^-CD31^-Sca1^+CD24^+$ MSCs. These results are consistent with our observation that sensory nerve regulation of bone homeostasis occurs only in adult mice, and not during development stages. The increase of adipogenesis after sensory denervation is also consistent with the high adipogenic potential of $LepR^+$ MSCs. Indeed, our fate mapping result validates that increased adipocytes in sensory denervation mice were the descendants of $LepR^+$ MSCs, considering that inhibition of sympathetic activity affected differentiation of $LepR^+$ MSCs in both sensory denervation mice and their WT littermates. Sensory nerve regulation of bone homeostasis is primarily through $LepR^+$ MSCs in adult mouse bone marrow. To this end, we do not exclude the involvement of other sub-groups of MSCs such as $Nestin^+$ MSCs and $PDGF\alpha^+$ MSCs, however, nearly all $PDGF\alpha^+$ stromal cells are $LepR^+$ MSCs, and vice versa, in mice aged 2–4 months (42), whereas $Nestin^+$ MSCs are abundant in postnatal mice, and their frequency significantly decreases in adult mice (57).

Adipogenesis increased and osteogenesis decreased in $EP4_{Avil}^{-/-}$ mice, $TrkA_{Avil}^{-/-}$ mice, and $COX2_{OCN}^{-/-}$ mice, but this phenotype could be caused by fate commitment of MSCs or alteration

of progenitor cell proliferation. We have shown increased expression of adipogenic markers and decreased expression of osteogenic markers in uninduced MSCs in these knockout mice relative to control mice. BrdU experiments showed the frequency of $BrdU^+$ MSCs and $BrdU^+$ OPCs was significantly reduced in these knockout mice relative to control mice, while $BrdU^+$ APCs were unaffected. These results suggest that sensory nerve is essential in the maintenance of self-renewal of MSCs. Sensory nerve also regulates the balance of commitment of MSCs between osteogenic and adipogenic lineages in MSCs fate determination. Particularly, sensory nerve regulates the proliferation of OPCs, but not APCs, which is consistent with our previous findings that elevated sympathetic tone reduced the proliferation of $osterix^+$ osteoprogenitors (7). Therefore, these results reveal that sensory nerve regulates lineage commitment of MSCs and acts as a niche for their maintenance, likely by regulating sympathetic tone.

Methods

Mice and In Vivo Treatment

were purchased from the Jackson Laboratory. The *Advillin-Cre* (*Avil-Cre*) mouse strain was kindly provided by Xingzhong Dong (Department of Neuroscience, The Johns Hopkins University, Baltimore, USA). The *Osteocalcin-Cre* (*OCN-cre*) mice were obtained from Thomas J. Clemens (Department of Orthopaedic Surgery, The Johns Hopkins University, Baltimore, USA). The $TrkA^{fl/fl}$ mice were obtained from David D. Ginty (Department of Neurobiology, Harvard Medical School, Boston, USA). The $COX2^{fl/fl}$ mice were provided by Harvey Herschman (Department of Biological Chemistry, University of California, Los Angeles, USA). The $EP4^{fl/fl}$ mice were obtained from Brian L. Kelsall (Laboratory of Molecular Immunology, National Institutes of

Health, Bethesda, USA). The *iDTR*$^{fl/fl}$ mice and the transgenic LepR-Cre mice, which expressed Cre recombinase under the control of mouse leptin receptor promoter were purchased from the Jackson Laboratory (*iDTR*$^{fl/fl}$ stock No. LepR-Cre stock No. 008320). Heterozygous male *Avil-Cre* mice (female *Avil-Cre* mice were not used for breeding because of the risk of leakage of TrkA protein into the eggs) were crossed with a *TrkA*$^{fl/fl}$, *EP4*$^{fl/fl}$, or *iDTR*$^{fl/fl}$ mouse. The offspring were intercrossed to generate the following genotypes: wildtype (referred to as "WT" in the text), *Avil-Cre* (Cre recombinase expressed driven by Advillin promoter), *Avil-Cre::EP4*$^{fl/fl}$ (conditional deletion of the EP4 receptor in Advillin lineage cells, referred to as "*EP4*$_{Avil}^{-/-}$" in the text), *Avil-Cre::TrkA*$^{fl/fl}$ (referred to as "*TrkA*$_{Avil}^{-/-}$" in the text), and *Avil-Cre::iDTR*$^{fl/+}$ (referred to as "*iDTR*$_{Avil}^{+/-}$" in the text). To generate the inducible sensory denervation mouse model, we injected 8-week-old *iDTR*$_{Avil}^{+/-}$ mice with 1 μg /kg diphtheria toxin (DTX) 3 times a week for 4 consecutive weeks. Heterozygous *OCN-Cre* mice were crossed with a *COX2*$^{fl/fl}$ mouse; the offspring were intercrossed to generate the following genotypes: *WT*, *OCN-Cre,* and *OCN-Cre::COX2* $^{fl/fl}$ (referred to as "*COX2*$_{OCN}^{-/-}$" in the text). Heterozygous *OCN-cre* mice were crossed with an *EP4*$^{fl/fl}$ mouse, and the offspring were intercrossed to generate the following genotypes: *WT* (referred to as *EP4*$^{fl/fl}$) and *OCN-cre:: EP4*$^{fl/fl}$ (conditional deletion of EP4 receptor in osteocalcin lineage cells, referred to as "*EP4*$_{OCN}^{-/-}$" in the text). *LepR-cre;YFP* mice were crossed by Leptin Receptor (LepR)-crewith Rosa26-YFP mice. The genotypes of the mice were measured by PCR analyses of genomic DNA, which was extracted from mouse tails within the following primers: *Avil-Cre*: forward: CCCTGTTCACTGTGAGTAGG, Reverse: GCGATCCCTGAACATGTCCATC, *WT*:AGTATCTGGTAGGTGCTTCCAG; *OCN-Cre*: forward: CAAATAGCCCTGGCAGATTC,

Reverse: TGATACAAGGGACATCTTCC; EP4 loxP allele forward: TCTGTGAAGCGAGTCCTTAGGCT, Reverse: CGCACTCTCTCTCTCCCAAGGAA ; *COX2* loxP allele forward: AATTACTGCTGAAGCCCACC , Reverse: GAATCTCCTAGAACTGACTGG; *TrkA* loxP allele forward: AACAGTTTTGAGCATTTTCTATTGTTT, Reverse: CAAAGAAAACAGAAGAAAAATAATAC; *iDTR* loxP allele forward: GCGAAGAGTTTGTCCTCAACC, Reverse: AAAGTCGCTCTGAGTTGTTAT. All animals were maintained at the animal facility of The Johns Hopkins University School of Medicine. We all used male mice in our experiments. We obtained whole blood samples by cardiac puncture immediately after euthanasia. Serum was collected by centrifuge at 1500 rpm for 15 min and stored at −80℃ before analyses. Femurs, tibias, and urine of the mice were also collected.

The drugs and compounds used in this study are as follows: diphtheria toxin (DTX, Sigma-Aldrich, D0564), capsaicin (Sigma-Aldrich, M2028), propranolol (Sigma-Aldrich, 1576005), and SW033291 (Selleck, S7900). Dosages and time courses are noted in the corresponding text and figure legends.

μCT Analyses

The femurs were harvested from mice, and the soft tissue around the bone was removed, followed by fixation overnight using 4% paraformaldehyde. μCT analyses were performed by using a high-resolution μCT scanner (SkyScan, 1174). The voltage of the scanning procedure was 65 kv with a 153-μA current. The resolution was set to 8.7 μm per pixel. Reconstruction software (NRecon,

v1.6, SkyScan), data analysis software (CTAn, v1.9, SkyScan), and 3D model visualization software (CTVol, v2.0, SkyScan) were used to analyze the diaphyseal cortical bone and the metaphyseal trabecular bone parameters of the femurs. We created cross-sectional images of the femur to perform 2D analyses of cortical bone and 3D analyses of trabecular bone. The region of interest of the trabecular bone was drawn beginning from 5% of the femur length proximal to the distal metaphyseal growth plate and extending proximally for another 5% of the total femur length. The trabecular bone volume fraction (BV/TV), trabecular thickness (Tb. Th), trabecular number (Tb. N), and trabecular separation (Tb. Sp) were collected from the 3D analysis data and used to represent the trabecular bone parameters.

OsO_4 Staining and μCT Analysis

The femurs were harvested from mice, fixed in 4% phosphate-buffered paraformaldehyde for 48 hours, and decalcified for 2 weeks in 10% EDTA at 4°C. The proximal of femurs were cut off and discarded. We incubated the distal part of femurs in 2% aqueous osmium tetroxide (OsO_4, Sigma-Aldrich) for 2 hours in the fume hood. The femurs were rinsed in phosphate buffered saline (PBS) for 48 hours and then scanned using a high-resolution μCT scanner (Skyscan 1172, Bruker MicroCT) at 6-μm resolution using 45 kVp and 177 μA. Quantification of number of adipocytes (Ad.N) and adipocyte volume/ marrow volume (Ad.V/ Ma.V) was registered to decalcified bone as previously described (58,59).

Histology, Immunohistochemistry and Immunofluorescence Assay

The femurs were collected and fixed in 4% paraformaldehyde overnight and decalcified by using 10% EDTA (pH, 7.4) (Amresco, 0105) for 21 days. The samples were then dehydrated with 30% sucrose for 24 hours and embedded in paraffin or optimal cutting temperature compound (Sakura Finetek). We prepared 4-μm-thick coronal-oriented sections of the femur for Safranin-O/ fast green (SO/FG) and Masson Staining according to the manufacture's protocols. Briefly, the sections were stained with Weigert iron hematoxylin for 5 mins, then counterstained with fast green for 3 mins, washed with 1% acetic acid, and stained in 0.1% SO, then the sections were dehydrated, cleared mounted, and visualized by light microscopy, the cartilage matrix proteoglycans stained red and bone compartments stained green coloration. For Masson staining, the sections were stained within Masson stain kit (Sigma-Aldrich, HT15), Cytoplasm and muscle fibers stained red and bone tissue displayed blue coloration. Thick sections were cut as described previously (42). Briefly, the femurs were fixed for 4 hours with 4% paraformaldehyde at 4°C and then decalcified at 4°C using 0.5 M EDTA (pH, 7.4) for 24 hours with constant shaking. The samples were dehydrated in 20% sucrose and 2% polyvinylpyrrolidone solution for 24 hours and embedded in 8% gelatin (Sigma-Aldrich, G1890) in the presence of 20% sucrose and 2% polyvinylpyrrolidone. Twenty and Forty-μm-thick coronal-oriented sections of the femurs were obtained, twenty μm thick sections for femur adipocytes and osteoblasts staining, Forty μm thick sections for femur sensory nerve staining.

Immunostaining was performed using standard protocol. Briefly, the sections were incubated with primary antibodies to osteocalcin (Takara Bio, M173, 1:200), Perilipin (Sigma, P1873, 1:500), CGRP (Abcam, ab81887), GFP (Abcam, ab13970), TrkA (R&D System, AF1065) overnight at 4℃. A horseradish peroxidase–streptavidin detection kit (Dako) was used in

immunohistochemical procedures to detect immuno-activity, followed by counterstaining with hematoxylin (Dako, S3309). Fluorescence-conjugated secondary antibodies were used in immunofluorescent procedures to detect fluorescent signals after counterstaining with DAPI (Vector, H-1200). We used a Zeiss LSM 780 confocal microscope or an Olympus BX51 microscope for sample image capturing. A BrdU staining kit (Thermo Fisher Scientific, 8800-6599-45) was used to perform the BrdU immunostaining procedure. Quantitative histomorphometric analysis was performed by using OsteoMeasure XP Software (OsteoMetric) in a blinded fashion.

Flow Cytometry Assay

Mice femurs were dissected and soft tissue of the femur was removed. We then crushed femurs with sterilized bone scissors, and the bone pieces were further digested within a 10-ml digesting buffer mixture of α-MEM containing 3 mg/ml collagenase I (Worthington), 4 mg/ml dispase (Sigma), and 1 U/ml DNase-I (Invitrogen) for 20 mins in a shaking water bath at 37℃. The suspension was passed through a 70-μm cell strainer to remove tissue fragments and then centrifuged at 300 g for 5 mins at 4℃. The pellet was resuspended in ACK lysing buffer (BD Bioscience) to exclude red blood cells and then centrifuged at 300 g for 5 mins at 4℃. The pellet was resuspended in 100 μl of staining buffer (Biolegend) and stained with antibodies for 30 mins at 4℃. The antibodies we used were as follows: Anti-CD31-Brilliant violet 421 (Biolegend, 102424, 1:200), Anti-CD45-Brilliant violet 421 (Biolegend, 103134, 1:200), Anti-Ter119-Brilliant violet 421 (Biolegend, 116234, 1:200), Anti-mouse Sca-1 APC/CY7 (Biolegend, 108126, 1:200),

Anti-CD24-PE (eBioscience,clone 30-F1, 1920468), and Anti-mouse CD140a (eBioscience, 135908). The dead cells were marked by using a fixable dead cell stain kit (Molecular Probes), and living cells were gated for lack of UV fluorescence. Before flow cytometry, cells were resuspended in staining buffer and analyzed on an LSR-II flow cytometer (BD Bioscience).

CFU-F, CFU-OB and CFU-AD in vitro differentiation assays

Bone marrow digestion and CFU-F, CFU-OB and CFU-AD assays of mouse bone marrow cells were based on previous described with customized (38,39). Briefly, For CFUs assays with unfractionated bone marrow cells, freshly isolated single cells suspension from 12-weeks old male mice's femur were plated at a density of $5 \times 10^4/cm^2$ in 6- well plates in DMEM (Gibco) with 15 % FBS (Gibco), 10 μmol/L Y-27632 (StemCell Technologies), and 1% penicillin/ streptomycin (Sigma-Aldrich), incubated at 37℃. For CFU-F assays with sorted cells, cells were sorted into cell culture at a density of 10 cells/cm^2 in 6- well plates, ensuring that colonies would form at clonal density to allow counting, CFU-F colonies were counted with Crystal violet staining after 10 days of expended, we counted the colonies that contained 50 cells or more. For the in vitro osteoblast differentiation assays (CFU-OB), cells were seeded at a density of $5 \times 10^3/cm^2$ and stained with Alizarin Red (Sigma-Aldrich) after 21 days cultured with osteogenic differentiation with STEMPRO Osteogenesis Differentiation Kits (Gibco). For in vitro adipocyte differentiation assays (CFU-AD), cells were seeded at a density of $1 \times 10^4/cm^2$ and stained with Oil Red (Sigma-Aldrich) after 14 days cultured with adipogenic differentiation with STEMPRO adipogenesis Differentiation Kit (Gibco).

505

506 **Quantitative Real-Time Polymerase Reaction Chain (qPCR)**

507 Total RNA was purified from cells in culture or tissues using TRIzol (Invitrogen, 15596026),
508 following the manufacturer's protocol. We performed qPCR using the Taq SYBR Green Power
509 PCR Master Mix (Invitrogen, A25777) on a CFX Connect instrument (Bio-Rad); *Gapdh*
510 amplification was used as an internal control. Dissociation curve analysis was performed for every
511 experiment. Sequences of the primers used for each gene are listed: *Pparg* forward:
512 ACCACTCGCATTCCTTTGAC, reverse: TGGGTCAGCTCTTGTGAATG. *Cebpa* forward:
513 AAACAACGCAACGTGGAGA, reverse: GCGGTCATTGTCACTGGTC. *Fabp4* forward:
514 CATCAGCGTAAATGGGGATT, reverse: GTCGTCTGCGGTGATTTCAT. *Alp* forward:
515 ATCTTTGGTCTGGCTCCCATG, reverse: TGAGCGACACGGACAAGAAGCCCTT. *Col1a1*
516 forward: GACGCCATCAAGGTCTACTG, reverse: ACGGGAATCCATCGGTCA. *Runx2*:
517 forward: TTACCTACACCCCGCCAGTC, reverse: TGCTGGTCTGGAAGGGTCC.

518

519 **In Vivo Incorporate BrdU Assay**

520 The BrdU assay was conducted as previously described (42). Briefly, mice were injected
521 intraperitoneally with a single dose of 100 mg/kg BrdU/ (Sigma) diluted in sterilized PBS. The
522 effect of BrdU labeling was maintained by giving BrdU via drinking water at a concentration of
523 0.5 mg/ml. Drinking water was renewed every other day. For BrdU analysis in flow cytometry, we
524 used an APC-BrdU flow kit (BD Bioscience) according to the manufacturer's instructions.

525

Bone Regeneration and Fracture Models

Mice underwent general anesthesia. The bone regeneration model was established as described previously (5). Briefly, a longitudinal incision was made on each knee to expose the femoral condyle by patella dislocation. Then, a hole was made at the intercondylar notch of the femur using a dental drill. A 0.6-mm-diameter Kirschner wire was placed from the proximal end of the femur to confirm marrow ablation by radiography. The dislocated patella was reposed, and the skin was sutured after removal of the Kirschner wire. Bone samples were harvested 7 days after bone marrow ablation, as described above.

The bone fracture procedure was performed as described previously (51). Briefly, after mice were anesthetized, a stainless-steel pin was inserted into the intramedullary canal from the distal femur to stabilize the fracture region. The pin was fixed in place by a wedge that was made by bending the first 2 mm of a 30-gauge needle. Fracture was made by 3-point bending, and the surgery region was then sutured. The treated mice were transferred into cages when they recovered from surgery and were checked twice a day. The fractured femurs were harvested, and the pin was removed 2 weeks postoperatively. μCT, bone sectioning, and staining were further performed on these bone samples.

Statistics

All data analyses were performed using SPSS, version 15.0, software (IBM Corp.). Data are presented as means ± standard errors of the mean (SEM). For comparisons between 2 groups, we used 2-tailed Student *t*-tests. For comparisons among multiple groups, we used 1-way analysis

of variance. A *P* value less than 0.05 was deemed significant. All representative experiments have been repeated at least three times. All relevant data are available from the authors.

Method for Von Frey test, hot plate test, kidney transplantation, metabolic studies and ELISA assay were described in the supplemental materials.

Study approval

All animal experiments were performed in accordance with NIH policies on the use of laboratory animals. All experimental protocols were approved by the Animal Care and Use Committee of The Johns Hopkins University.

Author contributions

B.H., and X.L. (Xiao Lv) performed most of the experiments. H.C. (Hao Chen), P.X., M.Y., B.G. and G.Z. helped with mice breeding and genotyping. P.W. and D.P. analyzed the μCT data. X.L. (Xiaonan Liu), Z.L. and J.C. helped with flow cytometry analysis. W.S, X.W. and S.L. performed the statistical analysis. R.D., S.N., and L.W. helped with mice breeding, genotyping, and euthanizing. Z.S., Y.Z. and H.C. (Huajiang Chen) offered equipment and valuable discussion. M.W., and W.Y. read and revised the manuscript. X.C. conceived the study and wrote the manuscript. The authorship order among co-first authors was determined by alphabetical sequence.

Acknowledgments

This research was supported by NIH grant AR 071432 (to XC). We thank editors Jenni Weems and

Rachel Box in the editorial office at the Department of Orthopaedic Surgery, The Johns Hopkins University, for editing the manuscript.

References

1. Snyder DJ, Bartoshuk LM. Oral sensory nerve damage: Causes and consequences. *Rev Endocr Metab Disord*. 2016;17(2):149-58.
2. Pinho-Ribeiro FA, Verri WJ, Chiu IM. Nociceptor Sensory Neuron-Immune Interactions in Pain and Inflammation. *Trends Immunol*. 2017;38(1):5-19.
3. Delmas P, Hao J, Rodat-Despoix L. Molecular mechanisms of mechanotransduction in mammalian sensory neurons. *Nat Rev Neurosci*. 2011;12(3):139-53.
4. Jung WC, Levesque JP, Ruitenberg MJ. It takes nerve to fight back: The significance of neural innervation of the bone marrow and spleen for immune function. *Semin Cell Dev Biol*. 2017;61:60-70.
5. Fukuda T, Takeda S, Xu R, et al. Sema3A regulates bone-mass accrual through sensory innervations. *Nature*. 2013;497(7450):490-3.
6. Takeda S, Elefteriou F, Levasseur R, et al. Leptin regulates bone formation via the sympathetic nervous system. *Cell*. 2002;111(3):305-17.
7. Chen H, Hu B, Lv X, et al. Prostaglandin E2 mediates sensory nerve regulation of bone homeostasis. *Nat Commun*. 2019;10(1):181.
8. Blackwell KA, Raisz LG, Pilbeam CC. Prostaglandins in bone: bad cop, good cop? *Trends Endocrinol Metab*. 2010;21(5):294-301.
9. Uppal S, Diggle CP, Carr IM, et al. Mutations in 15-hydroxyprostaglandin dehydrogenase cause primary hypertrophic osteoarthropathy. *Nat Genet*. 2008;40(6):789-93.
10. Kawabata A. Prostaglandin E2 and pain--an update. *Biol Pharm Bull*. 2011;34(8):1170-3.
11. Kuner R. Central mechanisms of pathological pain. *Nat Med*. 2010;16(11):1258-66.
12. Zhang Y, Desai A, Yang SY, et al. TISSUE REGENERATION. Inhibition of the prostaglandin-degrading enzyme 15-PGDH potentiates tissue regeneration. *Science*. 2015;348(6240):aaa2340.
13. Minamizaki T, Yoshiko Y, Kozai K, Aubin JE, Maeda N. EP2 and EP4 receptors differentially mediate MAPK pathways underlying anabolic actions of prostaglandin E2 on bone formation in rat calvaria cell cultures. *Bone*. 2009;44(6):1177-85.
14. Gao Q, Xu M, Alander CB, et al. Effects of prostaglandin E2 on bone in mice in vivo. *Prostaglandins Other Lipid Mediat*. 2009;89(1-2):20-5.
15. Crane JL, Cao X. Bone marrow mesenchymal stem cells and TGF-beta signaling in bone remodeling. *J Clin Invest*. 2014;124(2):466-72.
16. Zhen G, Wen C, Jia X, et al. Inhibition of TGF-beta signaling in mesenchymal stem cells of subchondral bone attenuates osteoarthritis. *Nat Med*. 2013;19(6):704-12.
17. Tang Y, Wu X, Lei W, et al. TGF-beta1-induced migration of bone mesenchymal stem cells couples bone resorption with formation. *Nat Med*. 2009;15(7):757-65.
18. Xie H, Cui Z, Wang L, et al. PDGF-BB secreted by preosteoclasts induces angiogenesis during coupling with osteogenesis. *Nat Med*. 2014;20(11):1270-8.

19. Uccelli A, Moretta L, Pistoia V. Mesenchymal stem cells in health and disease. *Nat Rev Immunol*. 2008;8(9):726-36.
20. Ellies DL, Krumlauf R. Bone formation: The nuclear matrix reloaded. *Cell*. 2006;125(5):840-2.
21. Fridenshtein A, Petrakova KV, Kuralesova AI, Frolova GI. Precursor cells for osteogenic and hemopoietic tissues. Analysis of heterotopic transplants of bone marrow. *Tsitologiia*. 1968;10(5):557-67.
22. Bianco P. Bone and the hematopoietic niche: a tale of two stem cells. *Blood*. 2011;117(20):5281-8.
23. Park D, Spencer JA, Koh BI, et al. Endogenous bone marrow MSCs are dynamic, fate-restricted participants in bone maintenance and regeneration. *Cell Stem Cell*. 2012;10(3):259-72.
24. Mendelson A, Frenette PS. Hematopoietic stem cell niche maintenance during homeostasis and regeneration. *Nat Med*. 2014;20(8):833-46.
25. Morrison SJ, Scadden DT. The bone marrow niche for haematopoietic stem cells. *Nature*. 2014;505(7483):327-34.
26. Prockop DJ. Marrow stromal cells as stem cells for nonhematopoietic tissues. *Science*. 1997;276(5309):71-4.
27. Mendez-Ferrer S, Michurina TV, Ferraro F, et al. Mesenchymal and haematopoietic stem cells form a unique bone marrow niche. *Nature*. 2010;466(7308):829-34.
28. Schneider RK, Mullally A, Dugourd A, et al. Gli1(+) Mesenchymal Stromal Cells Are a Key Driver of Bone Marrow Fibrosis and an Important Cellular Therapeutic Target. *Cell Stem Cell*. 2018;23(2):308-309.
29. Decker M, Martinez-Morentin L, Wang G, et al. Leptin-receptor-expressing bone marrow stromal cells are myofibroblasts in primary myelofibrosis. *Nat Cell Biol*. 2017;19(6):677-688.
30. Abbuehl JP, Tatarova Z, Held W, Huelsken J. Long-Term Engraftment of Primary Bone Marrow Stromal Cells Repairs Niche Damage and Improves Hematopoietic Stem Cell Transplantation. *Cell Stem Cell*. 2017;21(2):241-255.e6.
31. Maryanovich M, Zahalka AH, Pierce H, et al. Adrenergic nerve degeneration in bone marrow drives aging of the hematopoietic stem cell niche. *Nat Med*. 2018;24(6):782-791.
32. Katayama Y, Battista M, Kao WM, et al. Signals from the sympathetic nervous system regulate hematopoietic stem cell egress from bone marrow. *Cell*. 2006;124(2):407-21.
33. Ambrosi TH, Scialdone A, Graja A, et al. Adipocyte Accumulation in the Bone Marrow during Obesity and Aging Impairs Stem Cell-Based Hematopoietic and Bone Regeneration. *Cell Stem Cell*. 2017;20(6):771-784.e6.
34. Guan M, Yao W, Liu R, et al. Directing mesenchymal stem cells to bone to augment bone formation and increase bone mass. *Nat Med*. 2012;18(3):456-62.
35. Worthley DL, Churchill M, Compton JT, et al. Gremlin 1 identifies a skeletal stem cell with bone, cartilage, and reticular stromal potential. *Cell*. 2015;160(1-2):269-84.
36. Chan CK, Seo EY, Chen JY, et al. Identification and specification of the mouse skeletal stem cell. *Cell*. 2015;160(1-2):285-98.
37. Yu B, Huo L, Liu Y, et al. PGC-1alpha Controls Skeletal Stem Cell Fate and Bone-Fat Balance in Osteoporosis and Skeletal Aging by Inducing TAZ. *Cell Stem Cell*. 2018;23(2):193-209.e5.
38. Chan C, Gulati GS, Sinha R, et al. Identification of the Human Skeletal Stem Cell. *Cell*. 2018;175(1):43-56.e21.
39. Wu X, Pang L, Lei W, et al. Inhibition of Sca-1-positive skeletal stem cell recruitment by alendronate blunts the anabolic effects of parathyroid hormone on bone remodeling. *Cell Stem Cell*. 2010;7(5):571-80.
40. Mizuhashi K, Ono W, Matsushita Y, et al. Resting zone of the growth plate houses a unique class of skeletal stem cells. *Nature*. 2018;563(7730):254-258.

41. Fan Y, Hanai JI, Le PT, et al. Parathyroid Hormone Directs Bone Marrow Mesenchymal Cell Fate. *Cell Metab*. 2017;25(3):661-672.
42. Zhou BO, Yue R, Murphy MM, Peyer JG, Morrison SJ. Leptin-receptor-expressing mesenchymal stromal cells represent the main source of bone formed by adult bone marrow. *Cell Stem Cell*. 2014;15(2):154-68.
43. Yue R, Zhou BO, Shimada IS, Zhao Z, Morrison SJ. Leptin Receptor Promotes Adipogenesis and Reduces Osteogenesis by Regulating Mesenchymal Stromal Cells in Adult Bone Marrow. *Cell Stem Cell*. 2016;18(6):782-96.
44. Shi Y, He G, Lee WC, et al. Gli1 identifies osteogenic progenitors for bone formation and fracture repair. *Nat Commun*. 2017;8(1):2043.
45. Mizoguchi T, Pinho S, Ahmed J, et al. Osterix marks distinct waves of primitive and definitive stromal progenitors during bone marrow development. *Dev Cell*. 2014;29(3):340-9.
46. Kfoury Y, Scadden DT. Mesenchymal cell contributions to the stem cell niche. *Cell Stem Cell*. 2015;16(3):239-53.
47. Ortuno MJ, Robinson ST, Subramanyam P, et al. Serotonin-reuptake inhibitors act centrally to cause bone loss in mice by counteracting a local anti-resorptive effect. *Nat Med*. 2016;22(10):1170-1179.
48. Elefteriou F, Ahn JD, Takeda S, et al. Leptin regulation of bone resorption by the sympathetic nervous system and CART. *Nature*. 2005;434(7032):514-20.
49. Han R, Kitlinska JB, Munday WR, Gallicano GI, Zukowska Z. Stress hormone epinephrine enhances adipogenesis in murine embryonic stem cells by up-regulating the neuropeptide Y system. *Plos One*. 2012;7(5):e36609.
50. Riesco N, Cernuda-Morollon E, Pascual J. Neuropeptides as a Marker for Chronic Headache. *Curr Pain Headache Rep*. 2017;21(4):18.
51. Zhang Y, Xu J, Ruan YC, et al. Implant-derived magnesium induces local neuronal production of CGRP to improve bone-fracture healing in rats. *Nat Med*. 2016;22(10):1160-1169.
52. Furuyashiki T, Narumiya S. Stress responses: the contribution of prostaglandin E(2) and its receptors. *Nat Rev Endocrinol*. 2011;7(3):163-75.
53. Yoshida K, Oida H, Kobayashi T, et al. Stimulation of bone formation and prevention of bone loss by prostaglandin E EP4 receptor activation. *Proc Natl Acad Sci U S A*. 2002;99(7):4580-5.
54. Gao Q, Zhan P, Alander CB, et al. Effects of global or targeted deletion of the EP4 receptor on the response of osteoblasts to prostaglandin in vitro and on bone histomorphometry in aged mice. *Bone*. 2009;45(1):98-103.
55. Zhao H, Feng J, Ho TV, et al. The suture provides a niche for mesenchymal stem cells of craniofacial bones. *Nat Cell Biol*. 2015;17(4):386-96.
56. Baryawno N, Przybylski D, Kowalczyk MS, et al. A Cellular Taxonomy of the Bone Marrow Stroma in Homeostasis and Leukemia. Cell. 2019;177(7):1915-1932.
57. Kunisaki Y, Bruns I, Scheiermann C, et al. Arteriolar niches maintain haematopoietic stem cell quiescence. Nature. 2013;502(7473):637-43.
58. Li CJ, Xiao Y, Yang M, et al. Long noncoding RNA Bmncr regulates mesenchymal stem cell fate during skeletal aging. *J Clin Invest*. 2018;128(12):5251-5266.
59. Xiao Z, Cao L, Liang Y, et al. Osteoblast-specific deletion of Pkd2 leads to low-turnover osteopenia and reduced bone marrow adiposity. *Plos One*. 2014;9(12):e114198.

Figure legends

Figure 1. Sensory Nerve Denervation Induces Adipogenesis of MSCs at the Expense of Osteogenesis

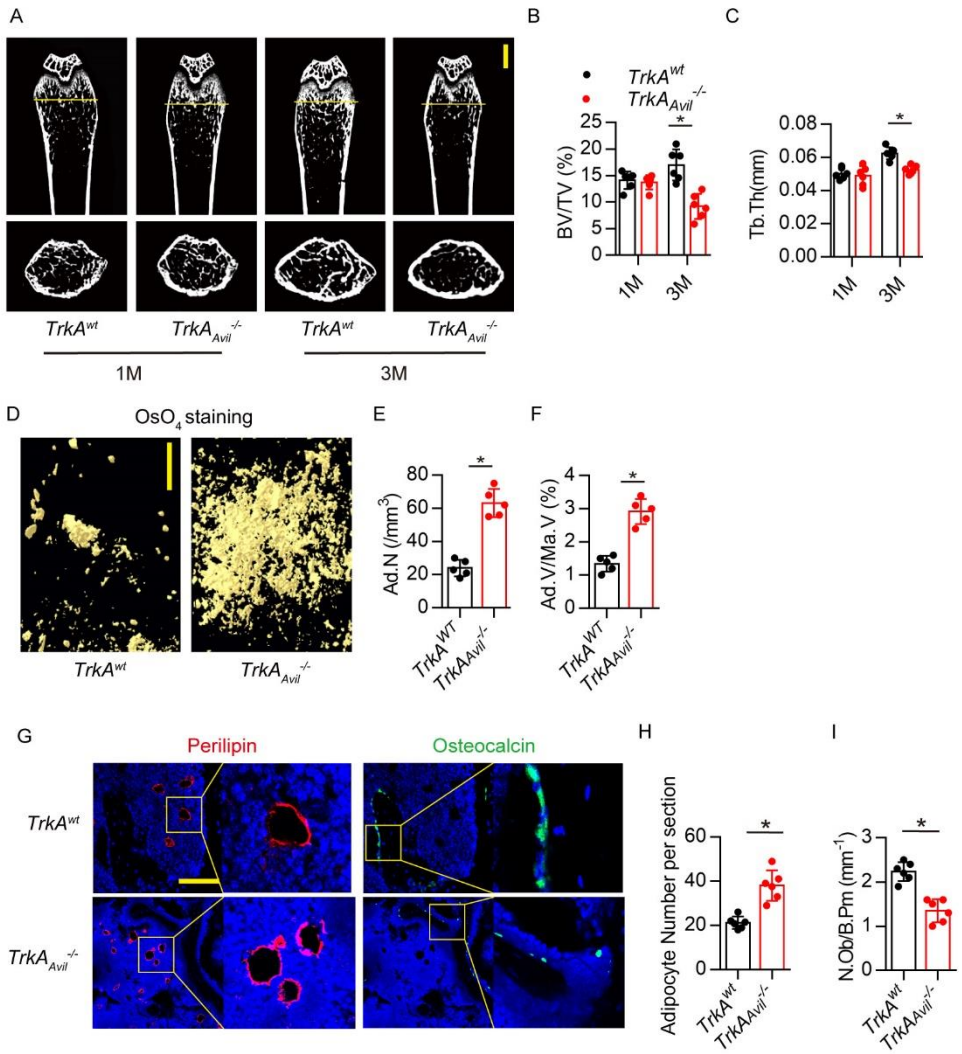

(A–C) Representative micro–computed tomography (μCT) images of femurs from 1-month-old and 3-month-old male *TrkA*^{wt} and *TrkA*$_{Avil}^{-/-}$ mice, the yellow line indicated the area where the cross-section images were captured (0.5 mm proximal from the growth plate). Quantitative analysis of trabecular bone fraction (Tb. BV/TV) and trabecular bone thickness (Tb.Th). Scale bar:

1 mm. (D–F) Representative μCT-detected osmium tetroxide (OsO_4)–stained images of decalcified femurs and quantitative analysis of number of adipocytes (Ad.N) and adipocyte volume/ marrow volume (Ad.V/ Ma.V) in distal femurs from 3-month-old male $TrkA^{wt}$ and $TrkA_{Avil}^{-/-}$ mice. Scale bar: 500 μm. (G–I) Representative images of immunofluorescence staining and quantitative analysis of the perilipin (red), osteocalcin (green)femurs from 3-month-old male $TrkA^{wt}$ and $TrkA_{Avil}^{-/-}$ mice. Scale bar: 50 μm. N≥6 per group, *P<0.05 (Student t-test).

Figure 2. MSCs Derived from Sensory Nerve Absence Mice Shifted to Adipogenesis

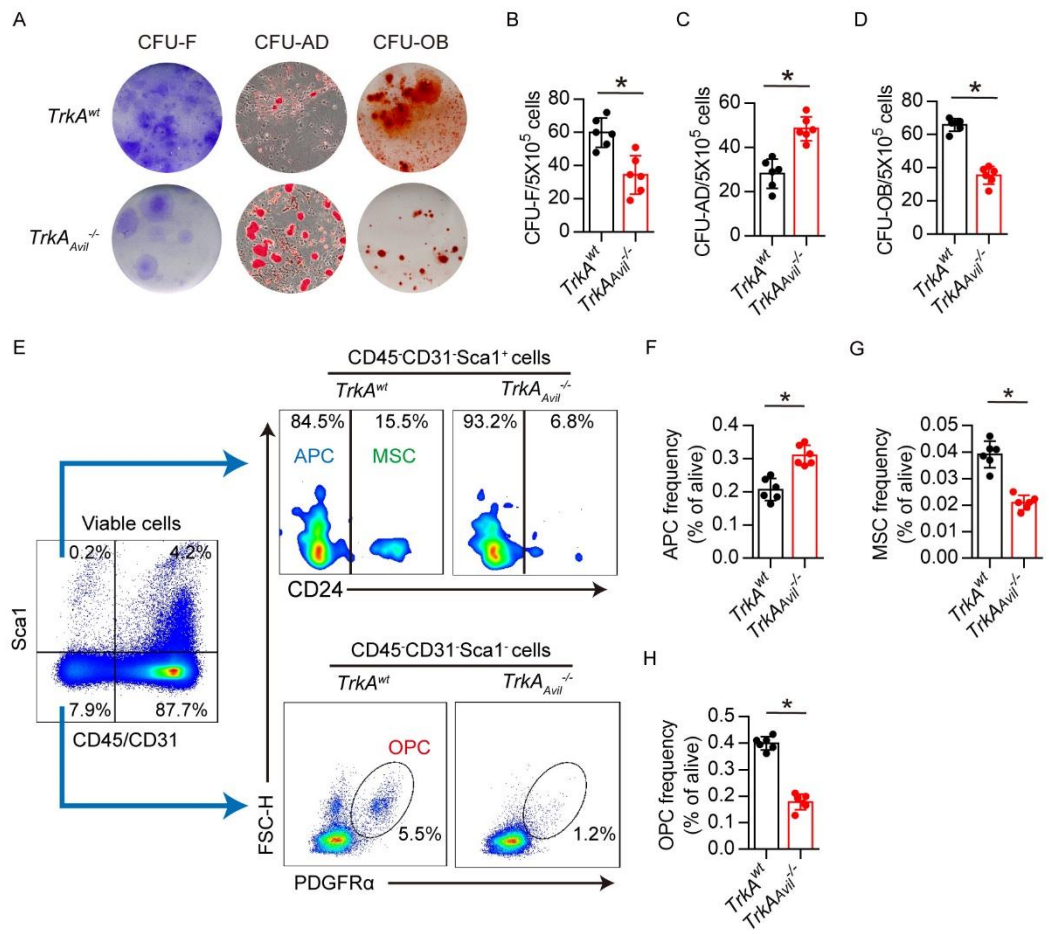

(A–D) Representative images of crystal violet–stained colony forming unit fibroblast (CFU-F), oil red O for adipocytes (CFU-AD), and alizarin red S (CFU-OB) for osteoblasts. Quantitative analysis of CFU-F, CFU-AD, and CFU-OB MSCs isolated from 3-month-old male *TrkA*^{wt} and *TrkA*$_{Avil}^{-/-}$ mice. (E–H) Representative dot plot images of flow cytometry and quantitative analysis of CD45$^-$CD31$^-$Sca1$^+$CD24$^-$ adipogenic progenitor cells (APCs), CD45$^-$CD31$^-$Sca1$^-$PDGFRα$^+$ (Pα$^+$) osteogenic progenitor cells (OPCs), and CD45$^-$CD31$^-$Sca1$^+$CD24$^+$ mesenchymal stromal cells (MSCs) of live cells isolated from femurs of 3-month-old male *TrkA*^{wt} and *TrkA*$_{Avil}^{-/-}$ mice. N ≥6 per group, **P*<0.05 (Student t-test).

Figure 3. Loss of Sensory Nerve Potentiates Adipogenesis

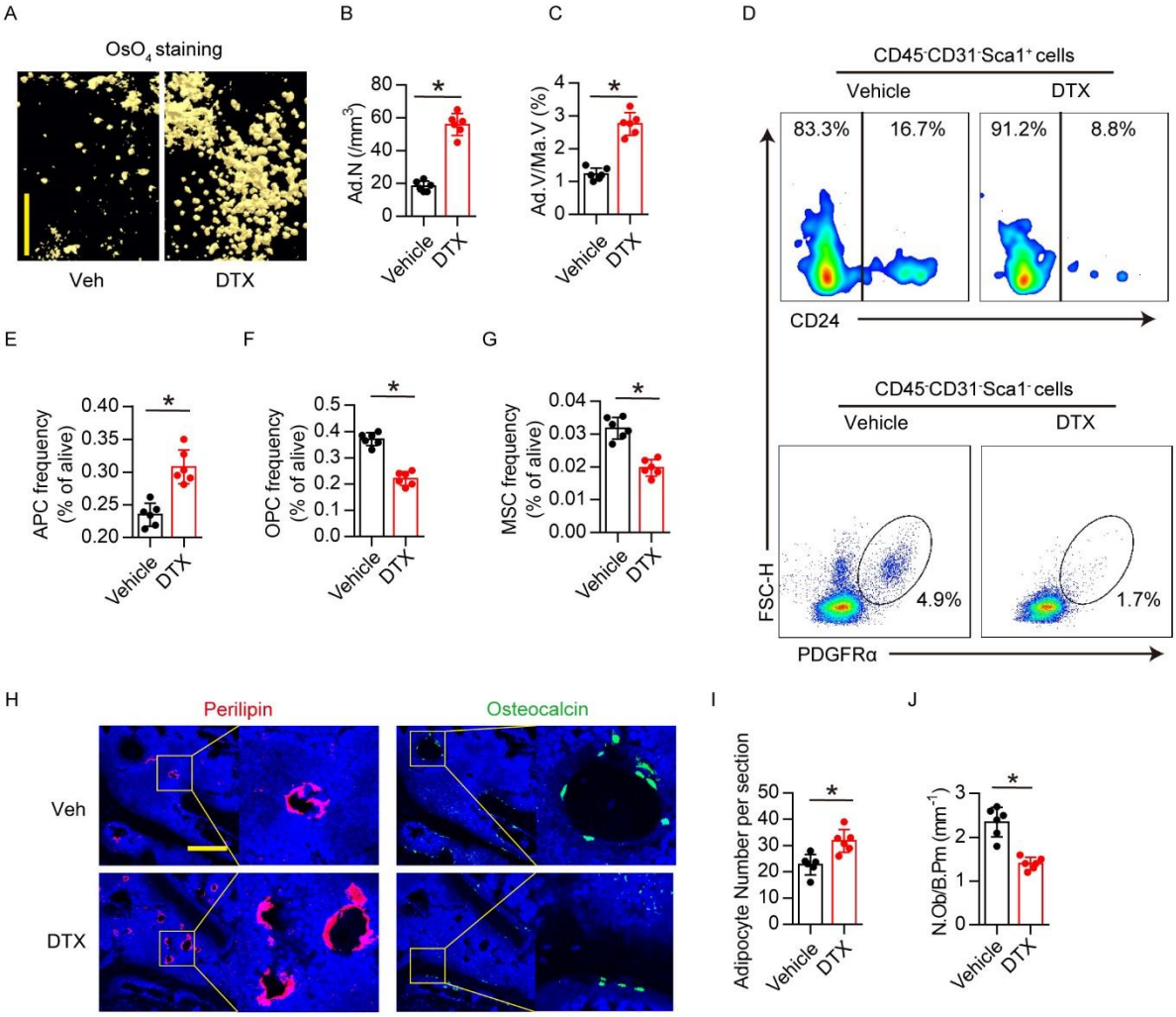

(A–C) Representative μCT-detected OsO_4-stained images of decalcified femurs and quantitative analysis of number of adipocytes (Ad.N) and adipocyte volume/ marrow volume (Ad.V/ Ma.V) in distal femurs of 3-month-old male *iDTR*$_{Avil}^{+/-}$ mice injected with 1ug per kg per day vehicle or diphtheria toxin (DTX) 3 time a week for four consecutive weeks. Scale bar: 500 μm. (D–G) Representative dot plot images of flow cytometry and quantitative analysis of $CD45^{-}CD31^{-}Sca1^{+}CD24^{-}$APCs, $CD45^{-}CD31^{-}Sca1^{-}PDGFR\alpha^{+}$ ($P\alpha^{+}$) OPCs, and $CD45^{-}CD31^{-}Sca1^{+}CD24^{+}$ MSCs of live cells isolated from femurs of 3-month-old *iDTR*$_{Avil}^{+/-}$ mice injected with vehicle or

DTX for 4 weeks. (H–J) Representative images of immunofluorescence staining and quantitative analysis of the perilipin (red), osteocalcin (green)in femurs from 3-month-old male *iDTR*$_{Avil}^{+/-}$ mice injected with vehicle or DTX for 4 weeks. Scale bar: 50 μm. N≥6 per group, **P*<0.05 (Student t-test).

Figure 4. Deletion of the EP4 Receptor in Sensory Nerve Promotes Adipogenesis and Inhibits Osteogenesis

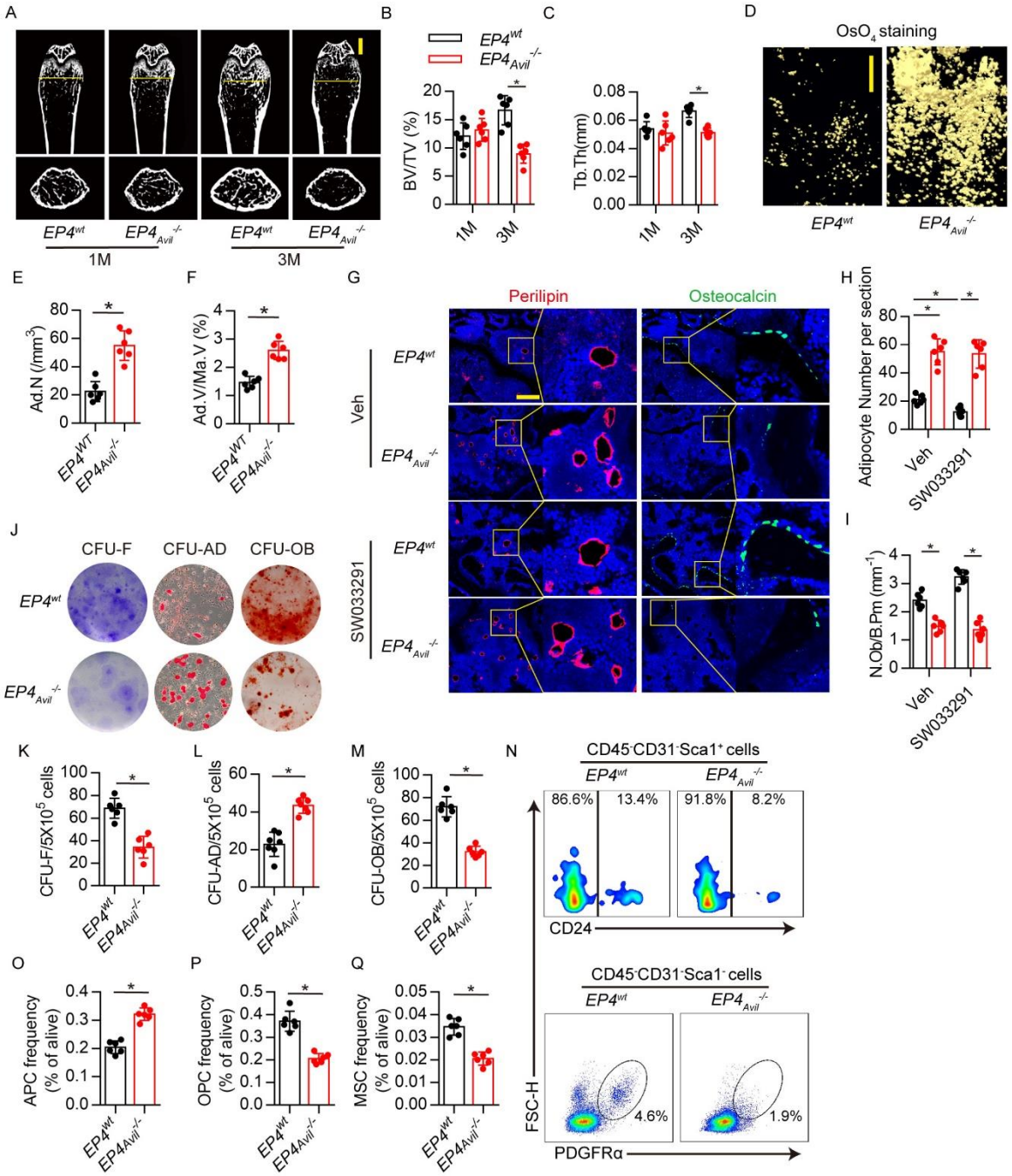

(A–C) Representative μCT images of femurs from 1-month-old and 3-month-old male *EP4*^{wt} and *EP4*$_{Avil}^{-/-}$ mice, the yellow line indicated the area where the cross-section images were captured

(0.5 mm proximal from the growth plate). Quantitative analysis of trabecular bone fraction (Tb. BV/TV) and trabecular bone thickness (Tb.Th). Scale bar: 1 mm. (D–F) Representative μCT-detected OsO_4-stained images of decalcified femurs and quantitative analysis of number of adipocytes (Ad.N) and adipocyte volume/ marrow volume (Ad.V/ Ma.V) in distal femurs from 3-month-old male $EP4^{wt}$ and $EP4_{Avil}^{-/-}$ mice. Scale bar: 500 μm. (G–I) Immunohistochemical staining of perilipin (red), osteocalcin (green)in femurs from 3-month-old male $EP4^{wt}$ and $EP4_{Avil}^{-/-}$ mice treated with SW033291 (10 mg per kg per day) and vehicle, respectively, for 1 month. Quantitative analysis of the density of perilipin and osteocalcin in femurs from 3-month-old male $EP4^{wt}$ and $EP4_{Avil}^{-/-}$ mice treated with SW033291 and vehicle, respectively, for 1 month. Scale bar: 50 μm. (J–M) Representative images of crystal violet–stained CFU-F, oil red O for adipocytes (CFU-AD), and alizarin red S for osteoblasts (CFU-OB). Quantitative analysis of CFU-F, CFU-AD, and CFU-OB MSCs isolated from 3-month-old male $EP4^{wt}$ and $EP4_{Avil}^{-/-}$ mice. (N-Q) Representative dot plot images of flow cytometry and quantitative analysis of $CD45^{-}CD31^{-}Sca1^{+}CD24^{-}$ APCs, $CD45^{-}CD31^{-}Sca1^{-}P\alpha^{+}$ OPCs, and $CD45^{-}CD31^{-}Sca1^{+}CD24^{+}$ MSCs of live cells isolated from femurs of 3-month-old male $EP4^{wt}$ and $EP4_{Avil}^{-/-}$ mice. $N \geqslant 6$ per group, $^{*}P<0.05$ (Student t-test).

Figure 5. PGE2 Derived from Osteoblasts Regulates the Differentiation of MSCs through EP4 in Sensory Nerve

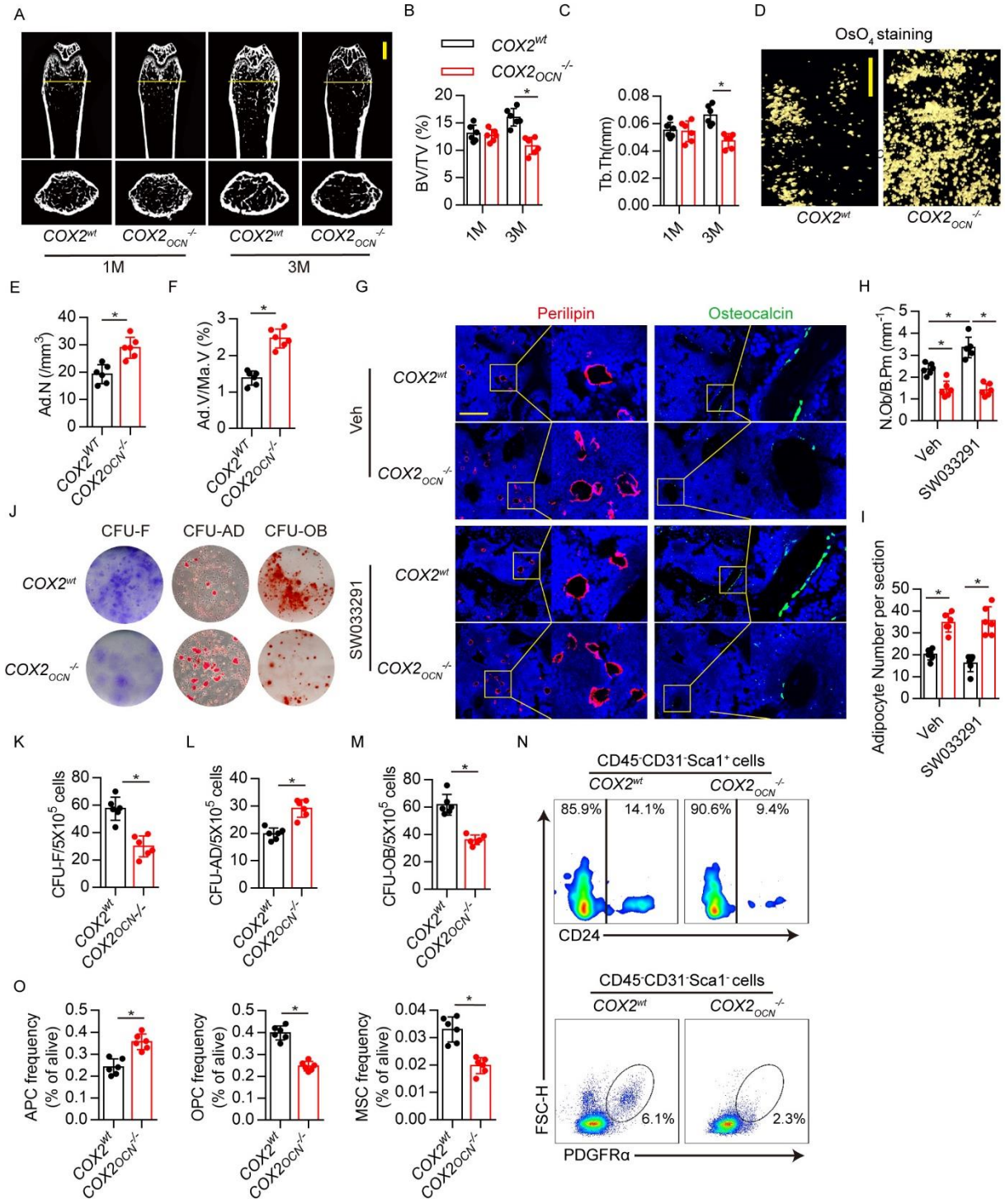

(A–C) Representative μCT images of femurs from 1-month-old and 3-month-old male *COX2*^{wt}

and $COX2_{OCN}^{-/-}$ mice, the yellow line indicated the area where the cross-section images were captured (0.5 mm proximal from the growth plate). Quantitative analysis of trabecular bone fraction (Tb. BV/TV) and trabecular bone thickness (Tb.Th). Scale bar: 1 mm. (D–F) Representative μCT-detected OsO_4-stained images of decalcified femurs and quantitative analysis of number of adipocytes (Ad.N) and adipocyte volume/ marrow volume (Ad.V/ Ma.V) in distal femurs of 3-month-old male $EP4^{wt}$ and $EP4_{Avil}^{-/-}$ mice. Scale bar: 500 μm. (G–I) Representative images of immunohistochemical staining of perilipin (red), osteocalcin (green)in femurs of 3-month-old male $COX2^{wt}$ and $COX2_{OCN}^{-/-}$ mice treated with SW033291 (10 mg per kg per day) and vehicle, respectively, for 1 month. Quantitative analysis of density of perilipin and osteocalcin in femurs of 3-month-old male $COX2^{wt}$ and $COX2_{OCN}^{-/-}$ mice treated with SW033291 and vehicle, respectively, for 1 month. Scale bar: 50 μm. (J–M) Representative images of crystal violet–stained CFU-F, oil red O for adipocytes (CFU-AD), and alizarin Red S for osteoblasts (CFU-OB). Quantitative analysis of CFU-F, CFU-AD, and CFU-OB MSCs isolated from 3-month-old male $COX2^{wt}$ and $COX2_{OCN}^{-/-}$ mice. (N-Q) Representative dot plot images of flow cytometry and quantitative analysis of $CD45^{-}CD31^{-}Sca1^{+}CD24^{-}$ APCs, $CD45^{-}CD31^{-}Sca1^{-}PDGFR\alpha^{+}$ ($P\alpha^{+}$) OPCs, and $CD45^{-}CD31^{-}Sca1^{+}CD24^{+}$ MSCs of live cells isolated from femurs of 3-month-old male $COX2^{wt}$ and $COX2_{OCN}^{-/-}$ mice. N≥6 per group, *P<0.05 (Student t-test for B, C, E, F, K-L and O-Q; two way ANOVA for H and I).

Figure 6. Capsaicin Induced Sensory Nerve Denervation Promote Adipogenesis And Inhibit Osteogenesis

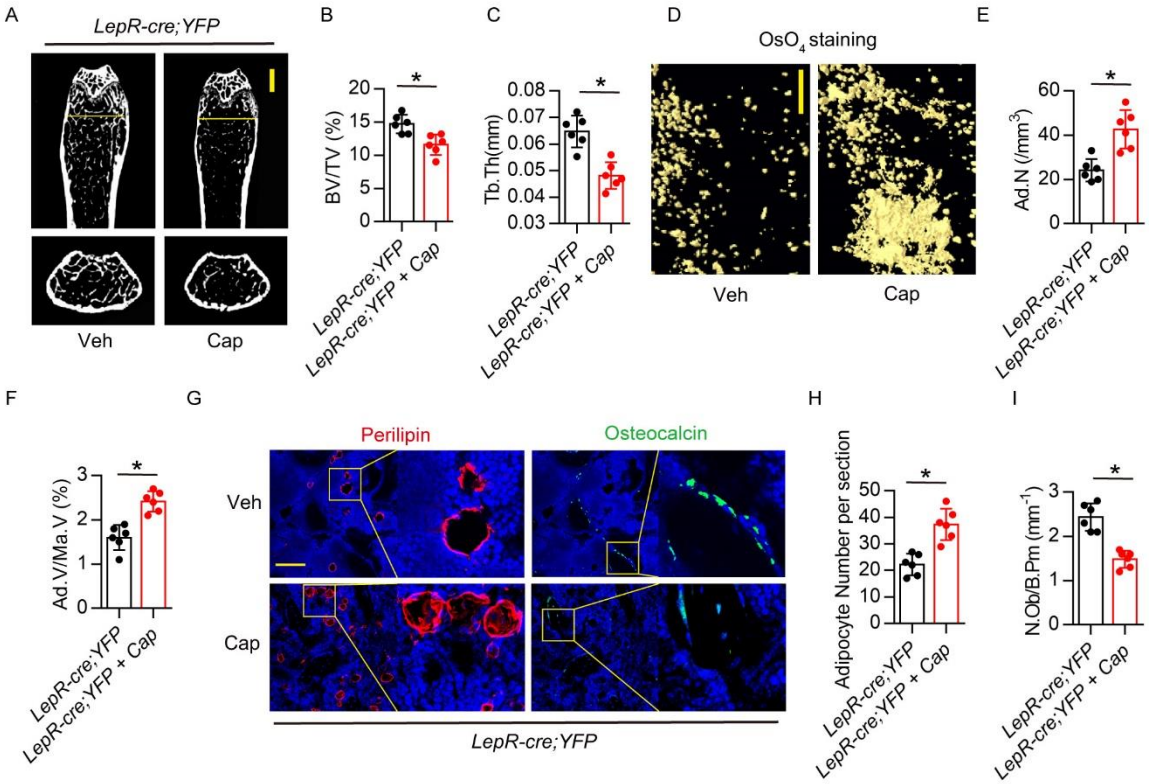

(A–C) Representative μCT images and quantitative analysis of trabecular bone fraction (Tb. BV/TV) and trabecular bone thickness (Tb.Th) of femurs from 3-month-old male *LepR-cre;YFP* mice injected with capsaicin (30 mg/kg per day) or vehicle for 1 week and euthanized after another 2 weeks, the yellow line indicated the area where the cross-section images were captured (0.5 mm proximal from the growth plate). Scale bar: 1 mm. (D–F) Representative μCT-detected OsO_4-stained images of decalcified femurs and quantitative analysis of number of adipocytes (Ad.N) and adipocyte volume/ marrow volume (Ad.V/ Ma.V) in distal femurs of 3-month-old male *LepR-cre;YFP* mice injected with capsaicin or vehicle for 1 week and euthanized after another 2 weeks. Scale bar: 500 μm. (G–I) Representative images of immunohistochemical staining of perilipin

(red), osteocalcin (green in femurs of 3-month-old male *LepR-cre;YFP* mice injected with capsaicin or vehicle for 1 week and euthanized after another 2 weeks. Scale bar: 50 μm. N⩾6 per group, **P*<0.05 (Student t-test).

Figure 7. LepR$^+$ MSCs are the Major Source of Increased Adipocytes that are Regulated by PGE2-EP4-Sensory Nerve Axis

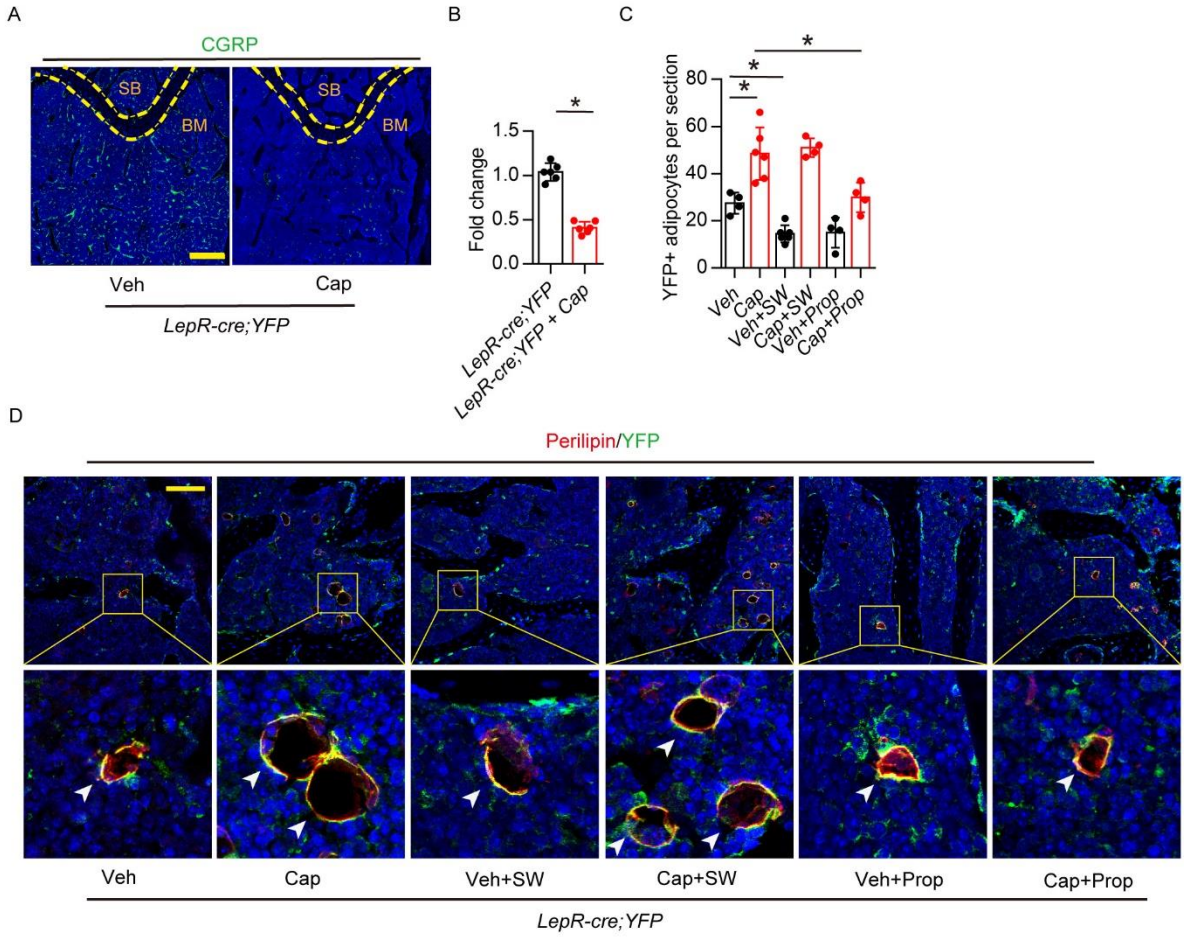

(A-B) Representative images of immunofluorescence staining and quantitative analysis of the CGRP$^+$ sensory nerves (green) in the distal femurs of 3-month-old male *LepR-cre;YFP* mice injected with capsaicin or vehicle for 1 week and euthanized after another 2 weeks, (Subchondral bone, SB; bone marrow, BM). Scale bar: 100 μm. (C) Representative images of immunofluorescence staining of co-localization of perilipin (red) and YFP (Representing LepR$^+$ cells) (green) in femurs bone marrow from 3-month old *LepR-cre;YFP* mice treated with capsaicin (30 mg per kg per day for 1 week), SW033291 (10 mg per kg per day for 1 month), or propranolol

(0.5 mg per kg per day for 6 weeks), and (D) quantitative analysis of YFP^+ adipocytes for each of the group (marrow adipocytes were labeled by white arrow). Scale bar: 50 μm. N⩾6 per group, *P<0.05 (Student t-test for B, two way ANOVA for D).

Figure 8. Impairment of EP4 Sensory Nerve Promotes Adipogenesis and Attenuates Bone Regeneration

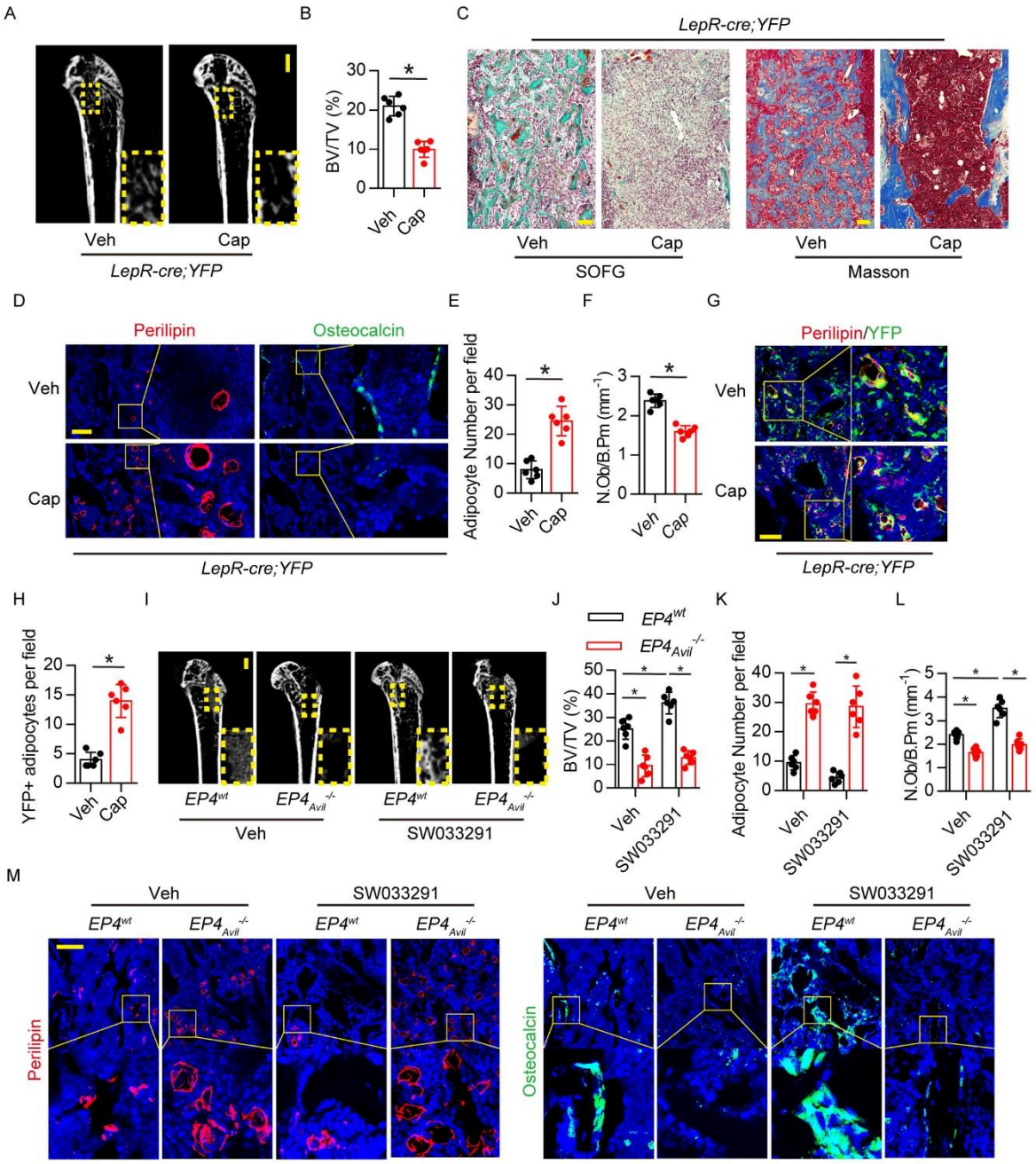

(A-B) Representative μCT images of bone regeneration after femoral bone marrow ablation in 3-month-old male *LepR-cre;YFP* mice treated with capsaicin (30 mg/kg per day) or vehicle 7 days

after bone marrow ablation. Scale bar: 1 mm. Selected areas for the measurements of BV/TV are indicated with a yellow square. (C) Representative SO/FG and Masson staining (red, muscle and cytoplasm; blue, bone) images in the regeneration area in 3-month-old male *LepR-cre;YFP* mice treated with capsaicin or vehicle 7 days after bone marrow ablation, red area represents as cartilage and green area represents as woven bone area in SO/FG staining, Scale bar: 100 μm. (D-F) Representative images and analysis of perilipin (red), osteocalcin (green) staining in the regeneration area from capsaicin treated group or controls. Scale bar: 50 μm. (G-H) Representative images of immunofluorescence staining of co-localization of perilipin (red) and YFP (representing $LepR^+$ cells) (green), and quantitative analysis density of YFP^+ adipocytes in the regeneration area from capsaicin treated group or controls. Scale bar: 100 μm. (I-J) Representative μCT images of bone regeneration after femoral bone marrow ablation in 3-month-old male $EP4^{wt}$ and $EP4_{Avil}^{-/-}$ mice treated with 10 mg per kg per day SW033291 or vehicle respectively 7 days after bone marrow ablation. Scale bar: 1 mm. Selected areas for the measurements of BV/TV are indicated with a yellow square. (K-M) Immunohistochemical staining and quantitative analysis of perilipin (red), osteocalcin (green) in the regeneration area from 3-month-old male $EP4^{wt}$ and $EP4_{Avil}^{-/-}$ mice treated with 10 mg per kg per day SW033291 or vehicle. Scale bar: 50 μm. N≥6 per group, *P<0.05 (Student t-test for B, E-F and H; two way ANOVA for J, L and M).

Figure 9. Sensory Nerve Denervation Impaired Bone Fracture Healing

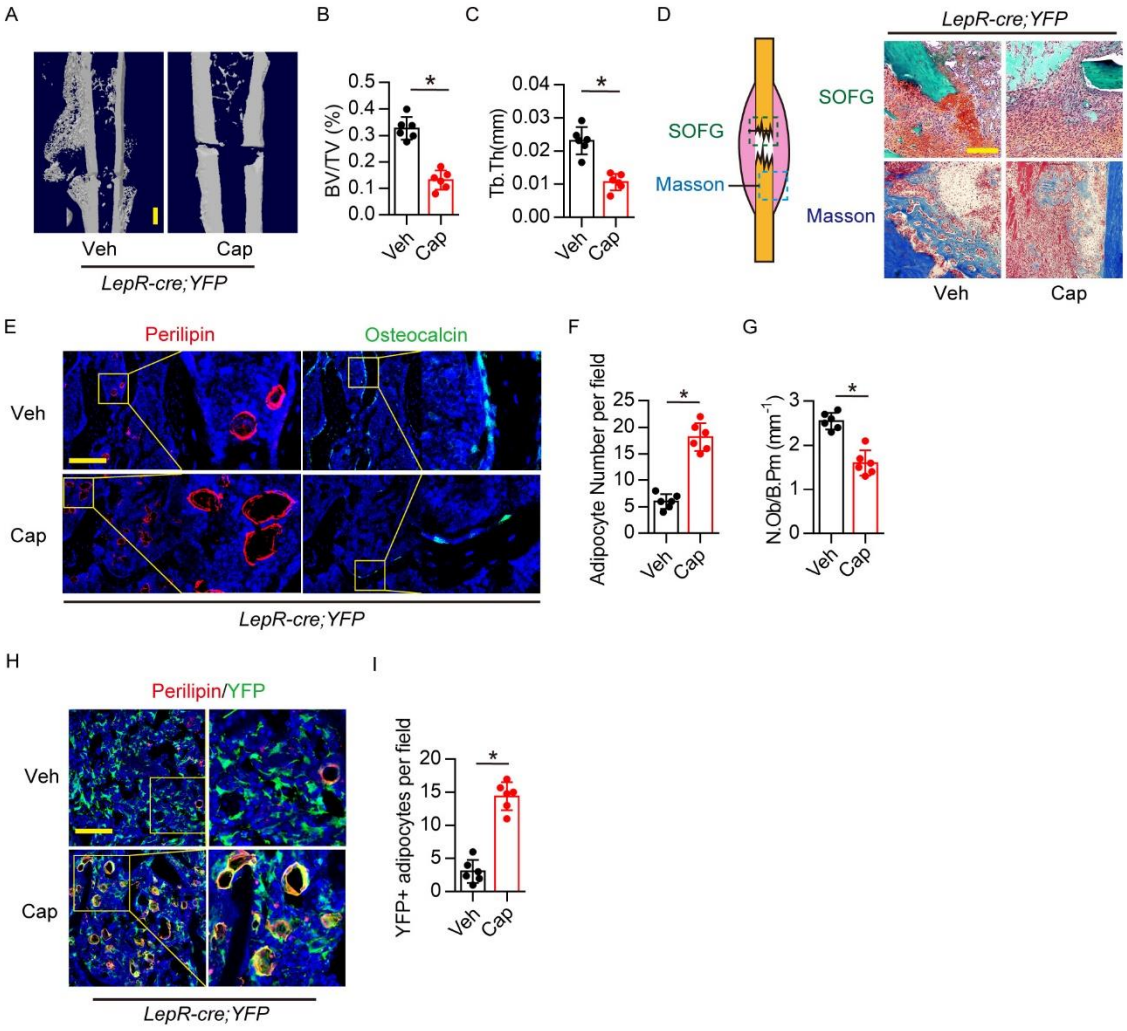

(A-C) Representative μCT images and quantitative analysis of BV/TV and Tb.Th of fracture healing area in 3-month-old male *LepR-cre;YFP* mice treated with capsaicin (30 mg/kg per day) or vehicle after bone fracture model created for 2 weeks. Scale bar: 1 mm. (D) Representative SO/FG (red, cartilage; green, bone) and Masson staining (red, muscle and cytoplasm; blue, bone) images in the fracture healing area in capsaicin treated group and control group. Scale bar: 100 μm. (E-G) Representative images of immunohistochemical staining and quantitative analysis of density of perilipin (red), osteocalcin (green) in fracture healing area in capsaicin treated group

and controls. Scale bar: 50 μm. (H-I) Representative images of immunofluorescence staining of co-localization of perilipin (red) and YFP (representing LepR+ cells) (green), and quantitative analysis of the density of YFP+ adipocytes in fracture healing area in capsaicin treated group and controls. Scale bar: 50 μm. N⩾5 per group, *P<0.05 (Student t-test).

Figure 10. Impairment of EP4 Sensory Nerve Interrupts Bone Fracture Healing

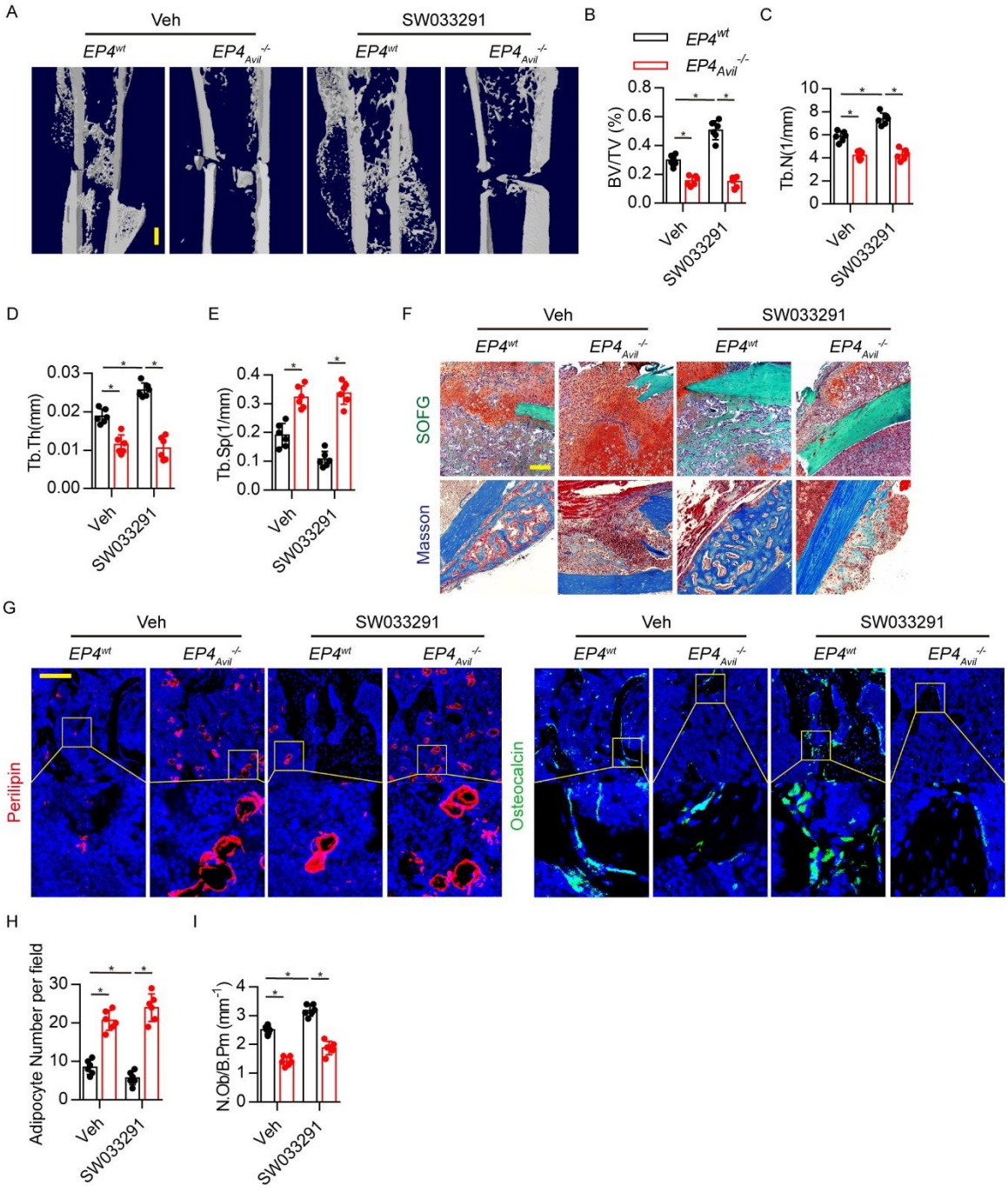

(A-E) Representative μCT images and quantitative analysis of BV/TV, Tb.Th, trabecular number (Tb.N) and trabecular separation (Tb.Sp) of bone fracture healing area in 3-month-old male $EP4^{wt}$ and $EP4_{Avil}^{-/-}$ mice treated with 10 mg per kg per day SW033291 and vehicle, respectively, after

bone fracture model created for 2 weeks. Scale bar: 2 mm. (F) Representative images SO/FG and Masson staining images in fracture healing area, and (G-I) immunohistochemical staining and quantitative analysis of perilipin (red), osteocalcin (green) in fracture healing area in 3-month-old male $EP4^{wt}$ and $EP4_{Avil}^{-/-}$ mice treated with SW033291 or vehicle respectively after bone fracture model created for 2 weeks. Scale bar: 50 μm. N≥5 per group, *P<0.05 (two way ANOVA).